Strontium and bisphosphonate coated iron foam scaffolds for osteoporotic fracture defect healing

Seemun Ray [a, 1], Ulrich Thormann [a, b, 1], Marlen Eichelroth [a], Matthäus Budak [a, b], Christoph Biehl [a, b], Markus Rupp [a, b], Ursula Sommer [a], Thaqif El Khassawna [a], Francisca I. Alagboso [a], Marian Kampschulte [c], Marcus Rohnke [d], Anja Henß [d], Klaus Peppler [d], Vanessa Linke [d], Peter Quadbeck [e], Axel Voigt [f], Florian Stenger [f], Daniel Karl [a], Reinhard Schnettler [a, b], Christian Heiss [a, b], Katrin S. Lips [a], Volker Alt [a, b, *]

[a] Laboratory of Experimental Trauma Surgery, Justus-Liebig-University, Giessen, Germany
[b] Department of Trauma Surgery, University Hospital Giessen-Marburg GmbH, Campus Giessen, Germany
[c] Department of Experimental Radiology, University Hospital Giessen-Marburg GmbH, Campus Giessen, Germany
[d] Institute of Physical Chemistry, Justus-Liebig-University Giessen, Giessen, Germany
[e] Fraunhofer Institute for Manufacturing Technologies and Advanced Materials IFAM, Branch Lab Dresden, Winterbergstraße 28, 01277, Germany
[f] Institute of Scientific Computing, Technische Universität Dresden, Zellescher Weg 12-14, 01069, Dresden, Germany

ARTICLE INFO

ABSTRACT

The purpose of this work was to investigate new bone formation in macroporous iron foams coated with strontium (FeSr) or bisphosphonate (FeBiP) compared to plain iron foam (Fe) and empty defect in a critical size metaphyseal bone defect model in ovariectomized rats. 60 female rats were subjected to bilateral ovariectomy and multi-deficient diet for 3 months. A 4 mm wedge shaped metaphyseal osteotomy was created, fixed with a mini-plate and subsequently filled with Fe, FeSr, FeBiP or left empty. After 6 weeks, µCt analysis revealed a statistically significant increased bone formation at the implant interface in FeSr compared to FeBiP (p = 0.035) and Fe (p = 0.002), respectively. Increased mineralized tissue was also seen within the pores in FeSr (p = 0.023) compared to Fe. Histomorphometry revealed significantly increased bone formation at the implant interface in FeSr (p < 0.001) and FeBiP (p = 0.006) compared to plain Fe with increased osteoblast and decreased osteoclast activity in combination with increased BMP2 and decreased RANKL/OPG in immunohistochemistry. ToF-SIMS analysis showed overlapping Ca signals with Fe for both FeSr and FeBiP thereby indicating tissue in-growth into the scaffolds. In conclusion, iron foam with strontium or bisphosphonate coating are of further interest in metaphyseal fracture defects in osteopenic bone.

© 2017 Published by Elsevier Ltd.

1. Introduction

The treatment of critical size fracture defects especially in diseased bone and aging population increases the demand for orthopedic reconstructions [1,2]. The pre-requisite for successful bone healing is the biomechanical stability of fracture defect, which is mainly provided by metallic fracture fixation devices, such as plates, nails or external fixators. As stability is mainly provided by these devices, scaffolds regardless of their mechanical stability can be implanted into the fracture defect. This includes not only the wide range of biodegradable polymer-based scaffolds (e.g. Collagen-GAG; Collagen-glycosaminoglycan) and ceramic-based scaffolds (e.g. CHA; collagen hydroxyapatite) [3,4] but also metallic material implants [5].

A further challenge is that healing rates vary with the diseased status of the bone as the rate of repair slows down. This is an important criterion to be taken into consideration, especially for enhancing osteogenesis [6]. Thus, ceramics e.g. calcium phosphates and bio glasses are widely used in bone repair which in turn can enhance the osteogenic potential of osteoblasts thereby enhancing

osteogenesis [7,8]. Secondly, alterations in vascularization network dramatically affect bone metabolism and health [9]. The use of growth factors, cells, and novel surgical are some of the recent approaches to improve neovascularization in polymer scaffolds for tissue engineering applications [10]. Last but not the least, tissue necrosis might also lead to implant failure thereby affecting healing.

Three metallic systems, based on magnesium (Mg), zinc (Zn) and iron (Fe) have been most widely used for orthopedic implants [11–17]. The non-toxicity and similarity in mechanical strength of Mg to human bone has made it most frequently used [2,18]. It is also necessary for the calcium incorporation into bone, and thus the release of magnesium ions is considered beneficial for bone healing [19,20]. However, the increased degradation rate and the fact that magnesium corrosion is linked to hydrogen evolution is a major drawback in the healing process [21,22]. Zinc not only plays an important role in stimulating bone formation, mineralization and plays a role in the preservation of bone mass but also acts as a selective inhibitor of osteoclastic bone resorption *in vitro* [23]. However, the lower mechanical strength is a major drawback. Iron of all not only shows better mechanical properties when compared to the others but also has a prolonged maintenance, thereby making it more suitable for higher load-bearing implants [12,24,25]. Also, its corrosion in body fluids does not lead to hydrogen ion evolution.

Iron plays a vital role in bone metabolism; however, its ferromagnetic behavior and substantially delayed degradation time are some of the difficulties with respect to its use in surgical applications. Despite the reported problems, *in vivo* use of pure iron as biodegradable cardiovascular stents has been shown to be safe [12,24,25]. Liu et al. also tested the *in-vitro* cytotoxicity of various iron alloys and reported no adverse effects [26]. This was further confirmed by Thompson and Puelo et al. in an *in vitro* study where osteogenic cells derived from bone marrow stromal cells, when subjected to sub-lethal solutions of metal ions for four weeks no toxic responses and decrease in cell number were observed [27]. Nie et al. also showed no *in vitro* toxic responses related to iron implants [28]. Despite this, limited studies on iron as a material to generate new bone formation has been carried out. Moreover, a surface oxide film formed on metallic materials play an important role as an inhibitor of the release of metallic ions and thus plays a very important role, not only for corrosion resistance (cytotoxic) but also for tissue compatibility. Hence, the use of a coating on the implants is preferable as it is known to reduce the corrosion rate and the cytotoxicity due to corrosion products. This was one of the rationales for the use of strontium and the bisphosphonate zoledronate coating on the iron foams.

The second rationale is to rebalance the bone turnover by creating an osteoconductive environment that allows tissue ingrowth [29]. In this study, we, therefore, combined open porous iron foam in combination with potential bone healing agents (strontium and zoledronate) in order to obtain a metal/drug composite material with increased initial load bearing capability and eventual fracture healing properties. Sr^{2+} with physical properties similar to Ca^{2+} allows it to be incorporated into the mineral phase of bone. Several studies have also shown the dual effects of stable strontium ions (Sr^{2+}) both *in-vitro* and *in-vivo* [30]. Our group also reported strontium modified calcium phosphate cement showed an enhanced bone formation [31]. Bisphosphonates (BiPs) on the other hand are shown to have high affinity to bone minerals resulting in their selective uptake by bone, mostly at regions of active bone remodeling which often gives rise to new bone formation [32]. Several studies have reported that local delivery of BiPs into diseased bones resulted in improved osseointegration of implants in osteoporotic animal models. In addition,

bisphosphonates are known to be anti-osteoclastic in nature [32,33]. The selected drugs resorb over a period of time and are known to support bony integration. Thus, the gradual replacement of these drugs with newly formed bone should thereby lead to a state of bio-hybrid composite of iron foam and bone.

The aim of the present work was to investigate the use of an iron scaffold as a potential carrier metal in a clinically relevant critical size metaphyseal defect in an ovariectomized rat model. Secondly, the effect of Sr and BiP coated iron on bone formation ability; biocompatibility and cytotoxicity have been also evaluated in this study.

2. Materials and methods

2.1. Ethics statement and animal study

After approval of the animal application by the local authorities according to the Protection of Animals Act (Reference number: V 54–19 c 20-15 (1) GI 20/28 Nr. 108/2011), 60 female Sprague-Dawley rats were used: 8 for μCt, histological, SEM-EDX and ToF-SIMS analysis and 7 for molecular analysis (per group). Each rat was randomly assigned to four different treatment groups: (1) empty defect pure (n = 15) (2) plain iron foam (Fe; n = 15), (3) strontium coated Fe foam (FeSr; n = 15), and (4) zoledronate (bisphosphate) coated Fe foam (FeBiP; n = 15). After six weeks, femurs were harvested for detailed investigations. In case of plate fixation failure, e.g. breakage or loosening, specimens were not taken for further analysis.

2.2. Preparation of macroporous iron scaffolds

Open cell iron foams were manufactured by replication method. Therefore, polyurethane templates (Foam partner Reisgies, Leverkusen, Germany) were coated using double rollers. Slurries containing water, polyvinyl-alcohol binder, and metal powders were used. In order to produce alloys with phosphorus contents of 0.6 wt.-%, carbonyl iron powder (BASF, Germany, mean particle size 4 μm) were mixed with Fe_3P particles (Atmix, Japan, mean particle size 1.5 μm) in a ratio of 96.2: 3.8. In the next step, the components were debindered at 500 °C in ArH_2-atmosphere and sintered at 1150 °C in pure hydrogen. Thus, open cell foam sheets (140 × 140 × 10 mm^3;) were produced. In the last step, v-shaped elliptical implants ($Ø_{large\ diameter}$ = 5 mm, $Ø_{small\ diameter}$ = 3 mm, h = 4.5 mm) were cut by wire EDM (Electrical discharge machining). In order to eliminate oxides caused by the cutting process, the implants were finally reduced to pure hydrogen at 800 °C.

The iron foams were coated with a) strontium salt precipitated from an aqueous $SrCO_3$, H_3PO_4 solution (FeSr) under vacuum conditions for 4 h (h) and maintained for additional 3 days at ambient conditions, finally rinsed with ethanol, and dried at 40 °C followed by gamma-irradiation for sterilization at 25 kGy resulting in a final average coating of 0.2 mg/cm^2 [Supplementary Method] b) zoledronic acid (FeBiP), a member of the bisphosphonate family. FeBiP was created by precipitation of zoledronic acid on iron. The foam was then carefully washed, dried, which finally resulted in a coating of 35 μg zoledronic acid on the basic iron foam. These three different formulations of bone substitution materials were implanted in the current animal model.

2.3. Animal surgery

10 weeks old female Sprague-Dawley rats were obtained from Charles River (Sulzfeld, Germany). Followed by an acclimatization period of four weeks, the animals were randomly assigned to four

treatment groups. Induction of an osteopenic bone status was achieved by bilateral ovariectomy using a dorsal approach and a low calcium-, phosphorous-, vitamin D3-, soy- and phytoestrogen-free multi deficient diet (Altromin-C1034, Altromin Spezialfutter GmbH, Lage, Germany) for 12 weeks. In comparison to the standard diet, the multi-deficient diet contained 0% vitamin D, 15% Calcium, 7% phosphorus, 50% vitamin K and 75% potassium as described previously [34]. After 12 weeks, a wedge-shaped defect was created as described by Alt et al. [35]. Briefly, after exposure of the lateral femur, a 7 hole T-shaped mini plate (Leibinger® XS-miniplate, Stryker®, Schönkirchen, Germany) was slightly bent and fixed to it with 1.7 mm screws. Two 8 mm screws perpendicular to the knee articular surface and one 8 mm screw inserted obliquely from a more proximal point through the femoral condyles were used to fix the plate to the distal femur. The proximal part of the plate was fixed with three 6 mm screws (Supplementary Figure S1). A wedge-shaped fracture-defect with a length of 4 mm and a medial gap of 0.35 mm was created at the distal metaphysis of the left femur using an ultrasound bone saw (Piezosurgery® 3, Saw blade OT7S-3, Mectron, Köln, Germany). The fracture-defect was either left empty or subsequently filled either with Fe foam, FeBiP or FeSr according to the randomization protocol. Multi-deficient diet was continued until euthanasia i.e. six weeks after femur surgery.

2.4. Sample processing

The femurs were harvested after six weeks and fixed in phosphate-buffered 4% paraformaldehyde for 48 h at 4 °C until processing. Samples were then embedded in Technovit® 9100 NEU according to the manufacturer's protocol (Heraeus Kulzer, Hanau, Germany). The same blocks were further used for µCT and histological analysis.

2.5. Micro-computed tomography (µCT)

Technovit embedded femora were scanned in a micro-CT System manufactured by Bruker micro-CT (SkyScan 1173, Bruker micro CT, Kontich, Belgium). Details concerning the scanning procedure are displayed in Table 1 according to the guidelines for assessment of bone microstructure described by Bouxsein et al. [36]. Aiming to reduce metal artifacts caused by the dense iron foam implants, an adjustment of our standard imaging protocol for the rat femur became mandatory. Therefore, a 1 mm Aluminium filter was used for beam filtration leading to reduced beam hardening artifacts. Furthermore, the combination of an elevated tube voltage as well as a high frame averaging (see Table 1) and a complete scanning (360°) resulted in a sufficient noise reduction, image contrast, and artifact suppression. Reconstructions were carried out using the NRecon-Software (Bruker micro CT, Kontich, Belgium), resulting in images of 8bit grayscale. Beam hardening correction was escalated to 45%. A Gaussian filter (smoothing kernel = 2, smoothing = 2) was employed for image reconstruction.

For the comparison of degraded vs. non-degraded materials, iron foam specimens were embedded in Technovit and scanned as well as reconstructed under the same conditions as the material containing femora (Table 1).

2.5.1. Post processing/data acquisition

A total of 70 slices/specimen from the midsagittal position of the femur as well as non-degraded iron foams were taken for image analysis, which was performed using the CTAn Software (Bruker micro CT, Kontich, Belgium). For the analysis of the new bone formation at the implant interface, the outer surface of the iron foam was manually contoured and it was expanded uniformly in all directions by a width of 210 µm in order to obtain the biomaterial interface. The cortical bone was also excluded from the VOI by manual contouring. For the calculation of the new bone formation within the iron foams, the outer boundaries of the iron foams were manually contoured. Iron foam intertwining within was removed from the ROI by means of global thresholding. The remaining tissue (defined as ROI) was thresholded using a global thresholding which was adapted to the mean density of the cortical bone to differentiate soft tissue (low density) from high dense materials (e.g. newly formed bone, iron remnants).

For the comparison of degraded vs. non-degraded materials, the ROI was defined as the area within the manually contoured outer surface of the iron foams. Segmentation was carried out using a global thresholding with same threshold values for all specimens. Morphometric analysis of the specimens comprised the 1. percent object volume (i.e. the percentage of metal within the foams), structure thickness and structure separation as a measure of material content and degradation.

2.6. Staining procedures and histomorphometry

Technovit® 9100 blocks were sectioned into 5 µm thick slices with the aid of Kawamoto's film (Section-Lab Co. Ltd., Japan) in order to avoid loss of biomaterials. Qualitative and quantitative morphological analyses were done on sections stained with movat-pentachrome and von Kossa/van Gieson as described earlier [37,38]. Qualitative differences in the morphology of osteocytes were evaluated on sections stained with silver as described previously [39].

For the histomorphometric analysis of new bone formation, osteoid formation, macrophage count and implant volume, 2 ROI's: ROI1 (user-defined) and ROI2 comprising of the initial wedge-shaped osteotomized defect area was used as described in detail previously [31]. For comparison of material degradation technovit embedded plain iron foam specimens were photographed and the percentage metal area was measured and compared to the experimental groups at 6 weeks using Photoshop.

The corroded surface layer was also evaluated. The 1st layer (direct proximity of metal implant) comprised the reddish brown hydroxide layer (Biocorrosion/Implant interface) and the 2nd layer consisted of the 1st layer plus the black grayish oxide layer (Biocorrosion/ROI). The layers evaluated are as described previously [40]. With the help of Adobe Photoshop CS6, the measurement for ROIs, area of bone, implant, osteoid, corrosion surfaces, and the void (sectioning artifacts) were made respectively to determine the ratio of bone volume over tissue volume (BV/TV), bone volume over implant volume (BV/IV), unmineralized tissue over ROI (UT/ROI), osteoid volume over tissue volume (OV/TV), biocorrosion over implant retention and biocorrosion over ROI. The measurements were done blind folded concerning the test groups.

Table 1
Details of the scanning procedure.

Tube voltage (kVp)	Tube current (µA)	Noise reduction (frame averaging)	Rotation steps (°)	Projections	Isotropic voxel sidel length (µm)
100	80	9-fold	0.25	1440 (360°)	14

2.7. Enzyme histochemical analysis

ALP staining was used to determine the osteoblast activity. After deplastification of the samples, they were incubated in a ready to use BCIP/NBT (Fa. KPL, 50-81-18) at 37 °C for 2 h. Counterstaining was done with Fast Red (Fa. Roth No. N069.1). Osteoblasts were traced on alkaline phosphatase stained slides as blue cuboidal cells aligned in clusters at the bone surface. The osteoblast surface over the bone surface (Ob.S/BS) was then determined by tracing directly on the osteoblast cells.

TRAP staining was used to investigate the osteoclast activity. The samples were deplastified, followed by treatment with sodium acetate buffer and incubation in Naphthol-AS-TR phosphate (N6125-1G, Sigma, Germany) in N–N-Dimethyl formamide (Sigma Aldrich) and sodium tartrate (Merck, Germany) with Fast Red TR salt (Sigma Aldrich) at 37 °C for 1 h.

Counterstaining was done with hematoxylin (Shandon Inc., Pittsburgh). A count of TRAP-positive cells (osteoclasts) was done in the fixed ROI in order to determine the osteoclast count per trabecular area (Oc./Tb. Ar).

2.8. Immunohistochemistry

Immunohistochemistry was carried out with the following antibodies: Rabbit Anti-BMP2 Polyclonal Antibody (AP20597PU-N; Acris), Rabbit Anti-Osteoprotegerin Polyclonal Antibody (250800; Abbiotec), Rabbit Anti CD254/RANKL Polyclonal Antibody (AP30826PU-N; Acris) and Monoclonal Mouse Anti-Human Muscle Actin (M0635; Dako) respectively.

Goat Anti-Rabbit (BA-1000, Vector) was used as a secondary antibody for BMP-2, OPG and RANKL followed by a Vectastain ABC kit (Elite PK-6100, Standard, Vector Laboratories, Burlingame, CA, USA). Finally, visualization was done using Nova Red (SK4800, Vector Laboratories, Burlingame, CA, USA) and hematoxylin (Shandon Inc., Pittsburgh, USA) was used as a counterstain. For ASMA, antigen identification was done using DakoEnvision + System-HRP (DAB) for use with mouse primary antibodies (Dako, K4006).

Images were taken using Axioplan 2 Imaging system (Carl Zeiss, Germany) with a Leica DC500 camera (Leica, Bensheim, Germany), acquired with Leica IM1000 software and processed using Adobe Photoshop CS6.

Qualitative and quantitative assessment of immunohistochemical staining was carried out to determine if the cells were positively stained against the background. For quantitative assessment, the entire original defect region was chosen and a Histo-score approach was utilized, where the fraction of negatively stained cells was given 0, weakly positive was given score 1, positive a score of 2, strongly positive a score of 3 and very strongly positive a score of 4 respectively. The fractions are then multiplied by the scores and summed up, the total being the H-score. The calculation was made according to the formula:

H Score = summation $(1 + i)$ pi where i is the intensity score and pi is the percent of the cells with that intensity.

2.9. mRNA preparation and gene expression analysis

The left femur was obtained 6 weeks after material implantation. Samples were snap frozen in RNA later® RNA Stabilization Solution (Ambion, CA, USA) and stored at −80 C until RNA isolation. The gene expression analysis was carried out for the following target genes as described in detail previously [31]:

(A) New bone formation: 1. Alkaline phosphatase (ALP), 2. Osteocalcin (OCN), 3. Collagen type10 alpha1 (Col10a1), 4. Runt-related transcription factor 2 (Runx2), 5. Collagen type I alpha1 (Col1a1).

(B) Bone resorption: 1. TNFSF11gene (RANKL, RANK ligand), 2. TNFRSF11B gene (osteoprotegerin; OPG), 3. Carbonic anhydrase, an osteoclast marker involved in bone matrix dissolution. β2-microglobulin (B2M) was used as a reference gene. The primer pairs are provided in the Supplemental Table S1. All analyses were done in duplicate and the mean was used for further calculations.

2.10. SEM/EDX

SEM/EDX measurements were conducted to characterize the materials used. The analysis was done using a high resolution scanning electron microscope "Merlin" from Carl Zeiss with a Schottky field emitter and a maximal spatial resolution of 0.8 nm. Micrographs were taken with two secondary electron detectors: an Everhart-Thornley detector (SE2) within the chamber and a semiconductor detector above the electron lens (InLens). The software used was SmartSEM (version 5.04) by Carl Zeiss Microscopy. For conductivity, the samples were coated previously with a thin layer of platinum in a sputter coater (Edwards Scancoat Six). SEM measurements were done for the implant materials at varying magnifications with a working distance between 2.9 mm and 3.9 mm. The beam current was 60 pA and the applied high voltage was 3 kV.

In addition, EDX mappings were done with an X-Max 50 detector (50 mm^2 detector area) from Oxford Instruments. For this analysis a working distance of 8.5 mm was chosen, the beam current was set to 120 pA and the high voltage applied was 10 kV. The software used for taking measurements was INCA (version 4.15) by Oxford Instruments and subsequently for analysis INCA and AZtec (version 3.2) also from Oxford Instruments. EDX measurements were done to determine the elemental composition of the samples at various spots and elemental distribution images were created for the tissue samples.

2.11. Computational model

The model as described before [41] was extended to 3D. Taking into consideration a diffusion problem for Sr^{2+} concentration in the foam with diffusion coefficient D = 10^{-8} cm^2/s, outflow boundary conditions on the inner surface were given by m'(t) = 0.61*10^{-7} mol/cm^2*(t/h)$^{-0.68}$ for t < 176.5 h and 0 afterwards and initial condition 0 everywhere. The release time and the flux result from the measured kinetics m(t) and the total amount of Sr^{2+} to be released was 1.0*10^{-6} mol/cm^2. The computational domain was chosen large enough and a no-flux condition was specified at the boundary. In order to deal with the complex foam structure in the simulation, a diffuse domain approximation [42] was considered. In this formulation, the geometry was only implicitly described by a phase field function, which was 1 in the pores, 0 in the solid part and smoothly varying within a small layer resolving the inner surface. The diffusion problem was extended to a larger simpler domain with the help of this phase field function and the outflow boundary condition was incorporated in the equations.

This formulation avoids meshing of the foam structure and allows to solve the problem using standard numerical tools, with the only requirement of an adaptive mesh refinement to resolve the diffuse inner surface. The system was solved using the Finite Element toolbox AMDiS [43,44] on the high-performance computer TAURUS at ZIH at TU Dresden. This approach requires various pre- and post-processing steps. The foam structure was obtained by μCT scans, which was segmented and described by a signed-distance

function, from which the phase field representation could be obtained and an appropriate mesh be constructed by adaptive refinement. To compute the overall flux from the foam we consider an additional phase field function, constructed as the envelope of the foam. The flux that results as the volume integral of the material flux was dotted with the gradient of this phase field function. The result as a function of time is shown in Fig. 7b and at t = 176.5 h in Fig. 7c, d.

2.12. ToF-SIMS measurements

5 μm thick slices of the embedded bone were deplastified with 2-methoxyethyl acetate (MERCK, Germany). SIMS measurements were performed with a ToF-SIMS 5−100 instrument (ION-TOF GmbH, Muenster, Germany), equipped with a 25 kV Bi-cluster primary ion source. For data analysis, the software Surface Lab 6.3 (ION-TOF, Muenster, Germany) was used.

Overview images of the tissue slices were obtained through stage scans and the use of Bi_3^+ as primary ions in high current bunched (HC-BU) mode with a lateral resolution of about 10 μm. For each image ten scans with a patch size between 4500×5000 μm^2 and $12,500 \times 8000$ μm^2 respectively 464×522 pixels and 1276×812 pixels were done. Each sub-image was scanned ten times with one primary ion shot per pixel. For seven of the samples, two detail images were done in addition using Bi_3^+ as primary ions in low current bunched (LC-BU) mode with a lateral resolution of 2 μm. One of the images focuses on the center of the implant area, the other on the border area. Pixel number was 256×256 pixels, analyzed area 500×500 μm^2 with 250 scans per image. All samples were measured in positive mode and samples from sub group 11 also in negative mode. For calibration in a positive mode the ions H^+, H_2^+, C^+, and CH_3^+ were used for the stage scans and CH_3^+, $C_2H_5^+$, $C_3H_7^+$, $C_4H_9^+$ and $C_5H_{11}^+$ for the detailed images. A cycle time of 55 us to 65 us was chosen which corresponds to secondary ions detected in a mass range of $m/z = 1$ to 245, respectively 370. The analyzing current was between ca. 0.5 pA (end: 0.04) and 0.9 pA for the HC-BU mode and 0.3 pA−0.4 pA for the LC-BU mode. Measured data were as scaled to the sum of total counts and the peaks were chosen manually. The implant material samples could be glued to a sample holder without further pretreatment. For these additional experiments, the same ions were chosen for calibration as for the detailed images. In contrast, the measured area was 100×100 μm^2 (for one sample only 50×50 μm^2 made sense) which correspond to 128×128 pixels.

2.13. Statistical analysis

The data were checked for normal distribution and homoscedasticity. One-way ANOVA along with Tukey's multiple comparison tests was adopted to determine the variation between the groups in histomorphometric analyses. If the requirements did not comply nonparametric Mann-Whitney U test was performed. For relative gene expression analysis, Student's t-test was performed. All the statistical analysis was done using Graph Pad Prism 7 (Graph Pad Software Inc., USA) and SPSS V. 20.0 (SPSS Inc., USA). The asterisks indicate the significance level (*) $p < 0.05$, (**) $p < 0.01$ and (***) $p < 0.001$ respectively. P-values of less than 0.05 were chosen to indicate significance.

3. Results

3.1. Foam characterization

As can be seen from the SEM images in Fig. 1a) the iron foam has a connected pore structure with pore diameters of about 200 μm. In the case of pure iron, the surface is not completely smooth (Fig. 1b and c). There is a terrace like surface structure with a structuring in nanometer scale. In Table 2 EDX data of the raw material (foam) is given. In the SEM micrographs of the uncoated iron foam, some areas appear darker than others. EDX analysis reveals that in the darker areas high amounts of carbon are present. In the brighter areas, the carbon content is much lower.

In the case of the Sr salt coating (FeSr), a typical needle-like morphology of precipitated inorganic salts is completely covering the surface (Fig. 1d). From EDX analysis of this material, it can be concluded that a mixed strontium carbonate phosphate precipitated during the coating process. According to Table 1 in addition to carbon also phosphorus together with a high amount of oxygen was detected in EDX analysis. The coating layer is about 10 μm thick. This can be estimated from weight gain and concluded by the fact, that also iron was detected in EDX. X-rays which are emitted due to electron impact usually originate from the first few micrometers of the near-surface region. In the very surface sensitive ToF-SIMS analysis, we observed a dense coating layer without iron signal.

As can be seen in Fig. 1e) and f) the precipitated zoledronate is forming a thin layer over the entire iron foam. Therefore, the terrace like surface of the pure iron foam cannot be seen as clearly as before. The iron content detected by EDX analysis is also higher for FeBiP (zoledronate) than coating with Sr carbonate phosphate (cf. Table 2). This suggests a thinner coating layer compared to FeSr. Comparable experiments with flat iron samples, we obtained a 1 μm thick layer for FeBiP.

3.2. Clinical observation

During the complete observation period 52 out of the 60 animals survived (n = 11; Empty defect, n = 15; Fe plain, n = 14; FeSr and n = 12; FeBiP respectively). 3 animals died during anesthesia, 3 died after ovariectomy and 2 died post-operatively. Wound healing and regain of mobility was documented during the observation period of 6 weeks. A gradual healing was observed in all the animals with no visible adverse effect in all the groups. At the time of femur harvest, plate breakage was detected in 2 of the remaining 11 in the empty defect group, 2 out of 15 in Fe plain, 3 animals out of remaining 14 in Fe plain compared to only one out of 14 in the FeBiP group and none in FeSr group. There were no significant differences in plate breakages in between empty compared to Fe (p = 0.7421), FeSr (p = 0.1040) and FeBiP (p = 0.494). However, a trend with less plate failure was seen in case of FeSr (0%) and FeBiP (8.3%) compared to plain Fe (13.3%) and empty defect (18.1%) respectively.

3.3. Radiographic analysis

Radiographic analysis revealed the highest amount of BV/TV in the FeSr group. Qualitative and quantitative analysis of the mineralized tissue at the implant interface suggested increased BV/TV in the FeSr group when compared to the plain iron foam (p = 0.002) (Fig. 2A; d, f). Also, an increase in BV/TV was seen in the same compared to FeBiP (p = 0.035) (Fig. 2A; e, f). In addition, a significant increase in the BV/TV was seen within the scaffold in the FeSr (p = 0.023) compared to the plain iron foam alone (Fig. 2B; g, i). Although no significant differences were seen in between FeBiP and FeSr, a trend more in favor of the latter was observed (Fig 2B; h, i). With respect to material degradation, no significant differences were seen in between the groups at 6 weeks. Also, no difference in material degradation was seen when the material remnant in Fe (p = 0.117), FeSr (p = 0.602) and FeBiP (p = 0.071) was compared to the starting material used (Supplementary Figure S3).
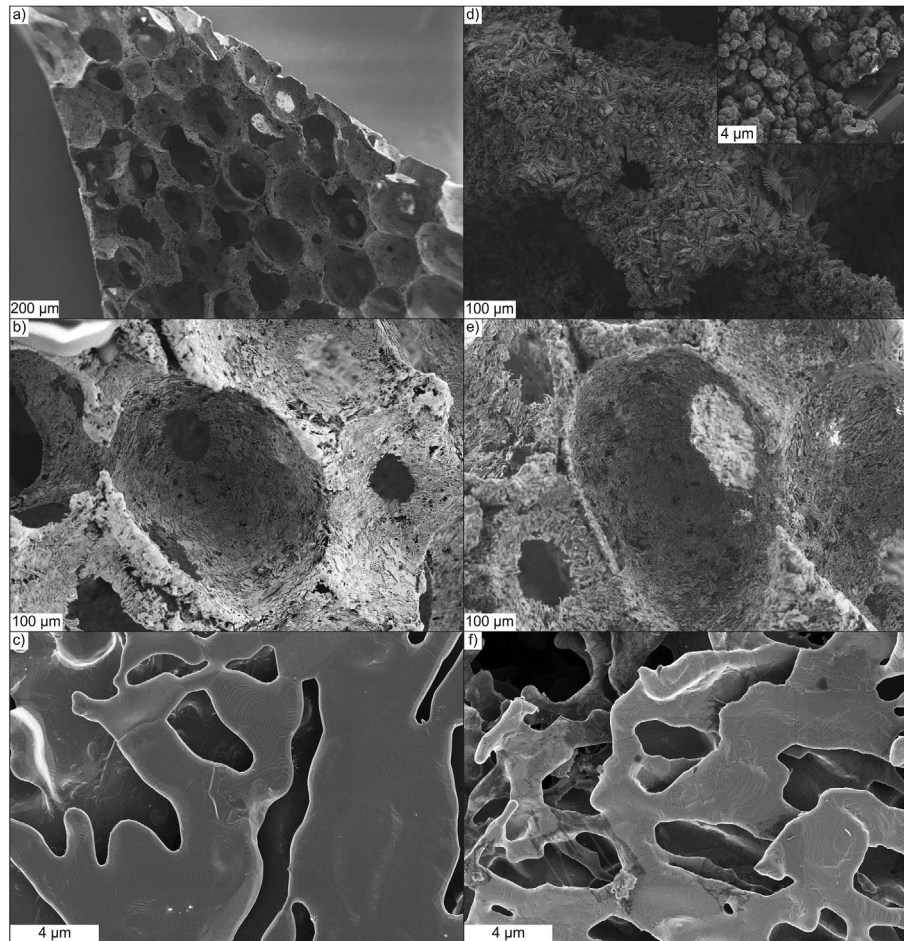
Fig. 1. SEM micrographs of the different samples. In a-c) images with different magnifications of the pure iron foam are shown. Fig. d) shows an image with an inset at higher magnification of the Sr salt coated foam. In e) and f) images of the zoledronate coated foam are depicted.

Table 2
EDX data of different areas of uncoated iron foam and coated iron foams. Detection limit of EDX is around 1 weight-% (depending on material). In this table elements were only traces were detected (values clearly below 1 weight-%) are omitted. Therefore, not all rows in weight-% do sum up to 100 weight-%. Rows with atomic-% are calculated from weight-% values given in this table, i.e. the sum is always 100 atomic-%.

Sample		C	O	P	Fe	Sr
Iron foam (bright area)	Weight-%	3	>1	>1	94	–/–
	Atomic-%	12.3	2.9	1.2	83.5	–/–
Iron foam (dark area)	Weight-%	42	>2	>1	55	–/–
	Atomic-%	75.9	2.3	0.2	21.7	–/–
Coated with Sr salt (needles)	Weight-%	4	30	13	31	22
	Atomic-%	9.3	54.7	12.0	16.5	7.6
Coated with Sr salt (lumps)	Weight-%	4	53	12	24	7
	Atomic-%	7.0	73.2	8.7	9.4	1.7
Coated with Bisphosphonate (bright area)	Weight-%	5	2–3	>1	90	–/–
	Atomic-%	19.3	7.1	1.3	72.3	–/–
Coated with Bisphosphonate (Fe/BiP, dark area)	Weight-%	43	3–4	>1	51	–/–
	Atomic-%	75,9	4,7	0,3	19,2	–/–
Coated with Bisphosphonate (Fe/BiP, dark area)	Weight-%	1–2	>1	>1	97	–/–
	Atomic-%	7,1	3,0	0,7	89,2	–/–

3.4. Descriptive histology

No biomaterial dislocation was observed. The implanted biomaterial was found in the correct position in the wedge-shaped defect where it was created initially at the distal metaphyseal femur region in all animals (Fig. 3a-c).

Unmineralized tissue, osteoid, and newly formed bone were found in the interface region, distal and in the mid-cortical around the implant. The maximum amount of newly formed bone and osteoid was seen in FeSr (Fig. 3g,k) and FeBiP (Fig. 3h,l) when compared to the other groups. Empty defect group revealed the highest area of granulation tissue (Fig. 3e). At the interface region was seen black, displaced iron particles which were phagocyted by macrophages. A brown zone surrounding the biomaterial was seen
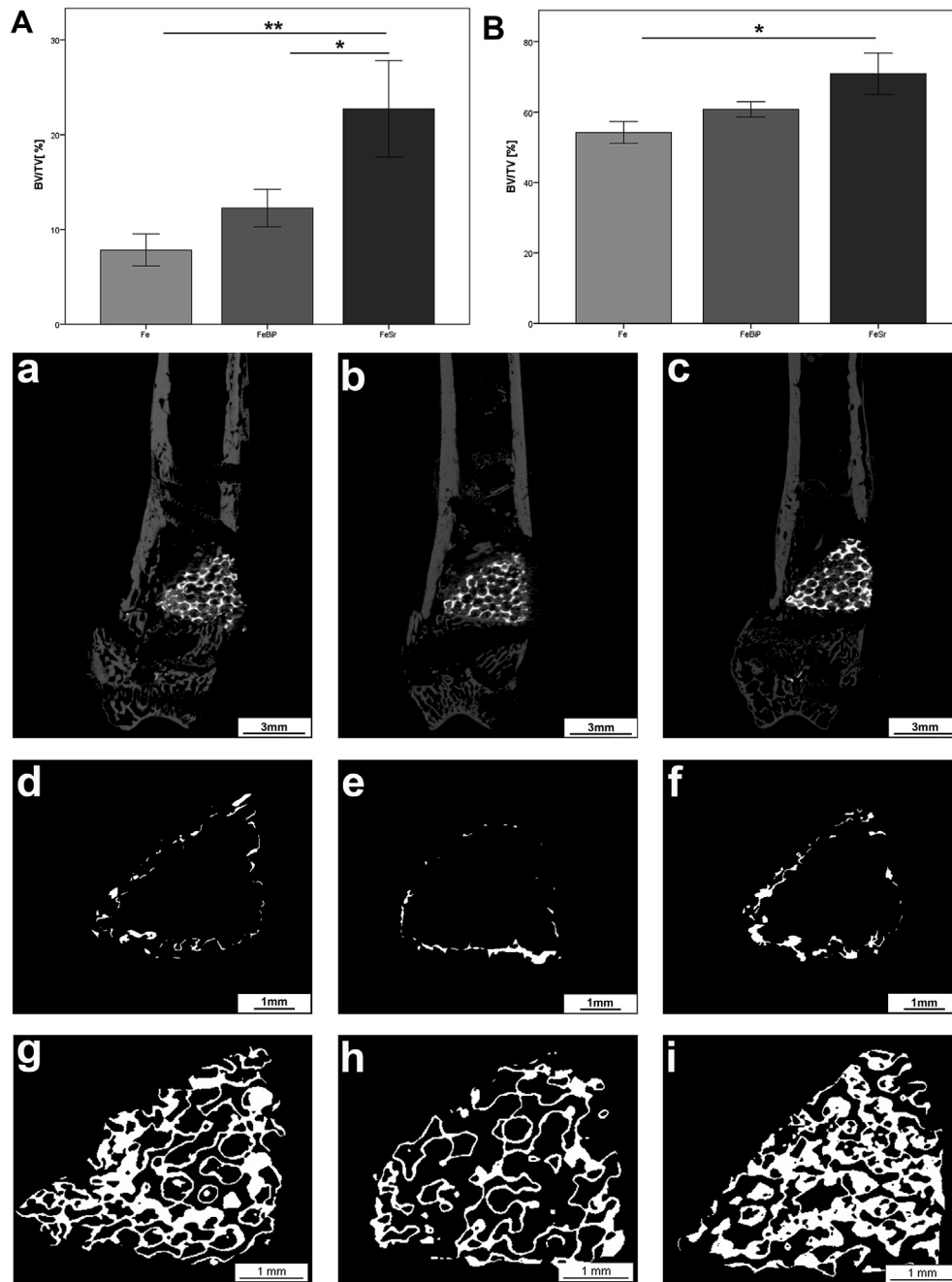
Fig. 2. Evaluation of new bone formation by quantitative μCT. Quantitative data of the μCT: bone volume fraction (BV/TV) at implant interface (A) and within the porous foam (B). 3D image reconstructions (longitudinal section) of Fe, FeBiP and FeSr (a,b,c). Scale bar = 1 mm. Transverse sections of Fe, FeBiP and FeSr showing increased bone formation at the implant interface in the FeSr group (f) compared to FeBiP(e) and plain Fe(d) group respectively. Increased bone formation in FeSr group (i) within the porous foam compared to other group (n = 8 each, Man Whitney; (*) p < 0.05, (**) p < 0.01 and (***) p < 0.001 respectively).

especially in Fe plain and FeBiP. Around these biomaterials, there was a degeneration zone formed consisting of necrotic macrophages. This degeneration zone seemed like a shell which inhibited the in-growth of granulation tissue. However this degeneration zone was absent in FeSr group, rather this was replaced by cells with brown cytoplasm in the interface region. Additionally, vessels with comparatively larger diameter were seen in FeSr group compared to the FeBiP group only (Supplementary Figure S4).

3.5. Histomorphometry

Histomorphometric analysis (ROI2) revealed a statistically significant increase in the bone formation (Bone volume/Tissue volume; BV/TV) in FeSr ($p = 0.001$) and FeBiP ($p = 0.001$) compared to the empty defect (Fig. 3A). However, no differences were seen in the empty group and the plain iron foam. There was also a statistically significant increase in bone formation (BV/TV) for FeSr ($p = 0.028$) and FeBiP ($p = 0.024$) in comparison to Fe plain alone. No statistically significant differences were seen in between FeSr and FeBiP group. At the implant interface (ROI1) a significant increase in bone formation (bone volume/implant volume; BV/IV) was seen in FeBiP (p = 0.006) and FeSr (p < 0.001) when compared to plain iron foam. No differences were seen in between FeBiP and FeSr alone (p = 0.107) (Fig. 3B). A significantly increased osteoid
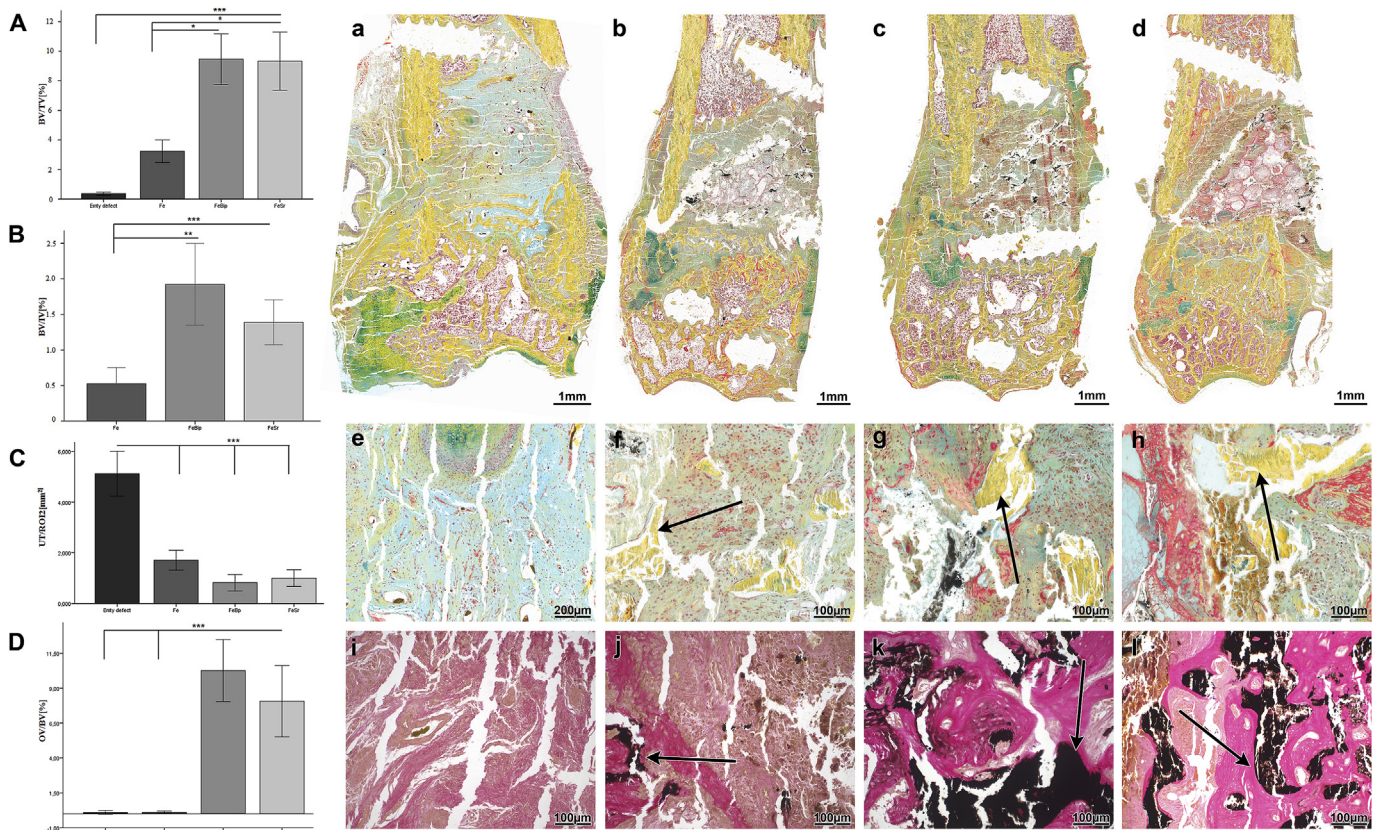
Fig. 3. Histomorphometrical analysis of BV/TV and OB/BV. Histomorphometrical analysis of new bone formation (BV/TV) in the initially created defect zone; ROI2 (A) and implant interface; ROI1 (B). Unmineralized tissue was significantly higher in the empty defect compared to other groups (C). Increased osteoid volume over bone volume (OB/BV) in FeBiP and FeSr compared to Fe and empty defect (D). Overview of movat pentachrome stained sections of empty, plain Fe, FeSr and FeBiP for histological analysis (a–d). Magnified images of the same showing increased bone formation (yellow) in FeSr and FeBiP (g,h) and Von Kossa Van Gieson staining showing increased osteoid (dark pink) in FeSr and FeBiP (k,l) compared to empty (e,i) and plain foam (f,j) respectively. (n = 8 each, One Way Anova; (*) p < 0.05, (**) p < 0.01 and (***) p < 0.001 respectively). (For interpretation of the references to color in this figure legend, the reader is referred to the Web version of this article.)

volume over bone volume (OV/BV in ROI2) was seen in the FeBiP and FeSr when compared to the empty defect and plain iron group respectively (p < 0.001) (Fig. 3D).

No significant differences were seen in the unmineralized tissue (ROI2) between the three groups (Fe, FeBiP, and FeSr). However, when compared to the empty defect a significant decrease was seen in the all the three groups (p < 0.001) (Fig. 3C).

The histomorphometric analysis also revealed no significant difference with respect to material degradation when the percentage of the metal area was compared in between the different test groups compared to the starting material (Supplementary Fig. S2). However, at 6 weeks a significant decrease was seen in FeSr (p = 0.002) and FeBiP (p = 0.003) compared to plain Fe foam (Supplementary Fig. S2). This could also be well co-related to the significant increase seen in biocorrosion at the implant interface in FeSr and FeBiP compared to plain iron foam (p < 0.001) (Supplementary Fig. S3). Also, biocorrosion in the entire ROI2 was highest in the FeBiP group compared to FeSr and plain Fe group respectively (p < 0.001) (Supplementary Fig. S3).

Osteoblasts, Osteoclasts, and Osteocytes.

The three main key players of bone remodeling i.e. osteoblasts, osteoclasts and osteocytes were assessed. The alkaline phosphatase staining showed a significant increase in the osteoblast activity in the FeBiP (p = 0.005) and FeSr (p < 0.001) when compared to the plain iron foam (Fig. 4A). Also, an increase in osteoblast activity was seen in the Fe (p = 0.07), FeBiP (p < 0.001) and FeSr (p = 0.003) when compared to empty defect group (Fig.4A; a-d).

Simultaneously, there was a significant decrease in the Oc. No/Tb.Ar in FeBiP and FeSr (p < 0.001) when compared to the empty and plain iron foam group respectively (Fig. 4B). Interestingly there was a significant higher Oc. No/Tb.Ar in the FeSr when compared to the FeBiP (p = 0.004) (Fig. 4B). Thus the least Oc. No/Tb.Ar was seen in case of the FeBiP (Fig. 4 B; e-h).
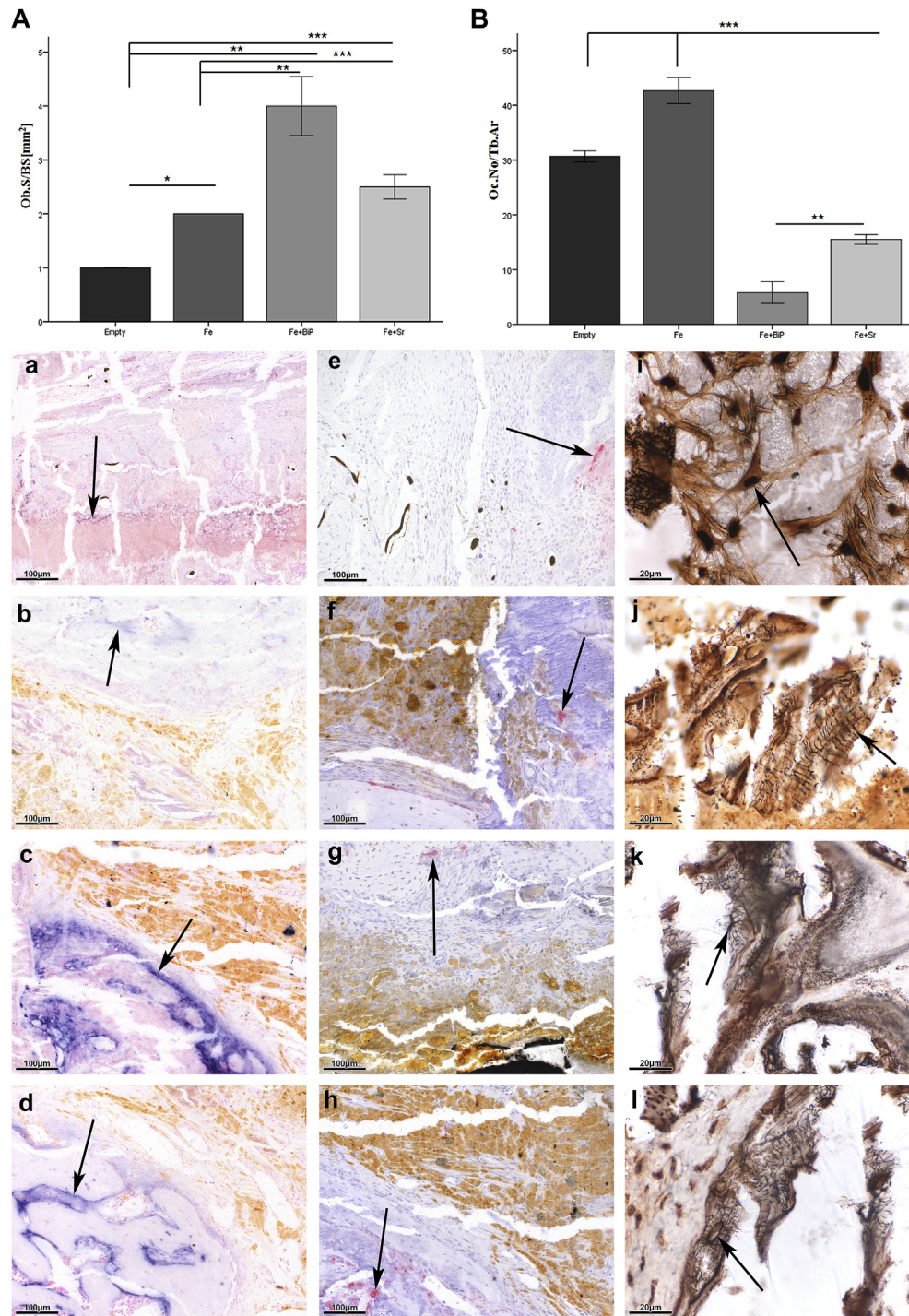
Staining for silver pigmentation for visualization of osteocytic lacunae canaliculi system (OLCS) of the surrounding bone around the implant after 6 weeks post-surgery revealed regular osteocytic canaliculi in FeBiP (Fig. 4k) and FeSr (Fig. 4l) as compared to the plain iron foam (Fig. 4j) and empty defect (Fig. 4i) where they were comparatively irregularly arranged with degenerated canaliculi. Also, the osteocytes were found in the direct vicinity of the materials in FeBiP and FeSr respectively whereas in case of the plain iron foam the degenerated osteocytes were mostly found in the oxidation zone. The damage of the osteocytic lacunae seems to be circumvented by the addition of Sr and BiP which display regular osteocytic canaliculi directly at the implant interface which displays regular osteocytic canaliculi directly at the implant interface (Fig. 4i-l).

3.6. Immuno histochemical analysis

3.6.1. Qualitative

Immunohistochemical staining revealed a strong positive BMP2 expression in the FeSr and FeBiP as compared to the plain iron foam. Similarly, an increased ALP expression was also seen in the

Fig. 4. Comparative histomorphometric analysis. Ob. S/BS based on ALP staining in the initially created defect zone (A). Macrophage count (Oc.No/Tb.Ar) based on TRAP staining in the same ROI (B). Photomicrographs of histologically stained sections with ALP staining showing increased expression in FeBiP (c) and FeSr (d) compared to empty (a) and plain iron (b). Simultaneous decrease in TRAP positive cells in FeBiP (g) and FeSr (h) compared to empty (e) and Fe (f). Staining for silver pigmentation for visualization of OLCS of the surrounding bone around implant after 6 weeks post surgery reveals regular osteocytic canaliculi in FeBiP (k) and FeSr (l) as compared to empty defect (i) and plain iron foam (j) respectively (i,j). (n = 8 each, Man Whitney; (*) p < 0.05, (**) p < 0.01 and (***) p < 0.001 respectively).

FeSr and FeBiP as compared to the plain iron foam (Fig. 5A). An increased OPG expression was seen at the distal and mid cortical region of the fracture gap with simultaneous down-regulation of RANKL in FeSr and FeBiP as compared to the plain iron foam (Fig. 5B). Although no difference in blood vessel formation was seen in between the groups, relatively smaller vessel size was observed in case of the FeBiP when compared to the other three groups.

3.6.2. Quantitative analysis

A Histo-score approach was used for immunohistomorphometry. A statistically significant increased BMP2 score was obtained for FeSr (0.002) and FeBiP (p = 0.004) when compared to the empty defect. The FeSr and FeBiP also had a statistically increased BMP2 score when compared to plain iron foam alone (p = 0.05) (Fig. 5A; a-d).
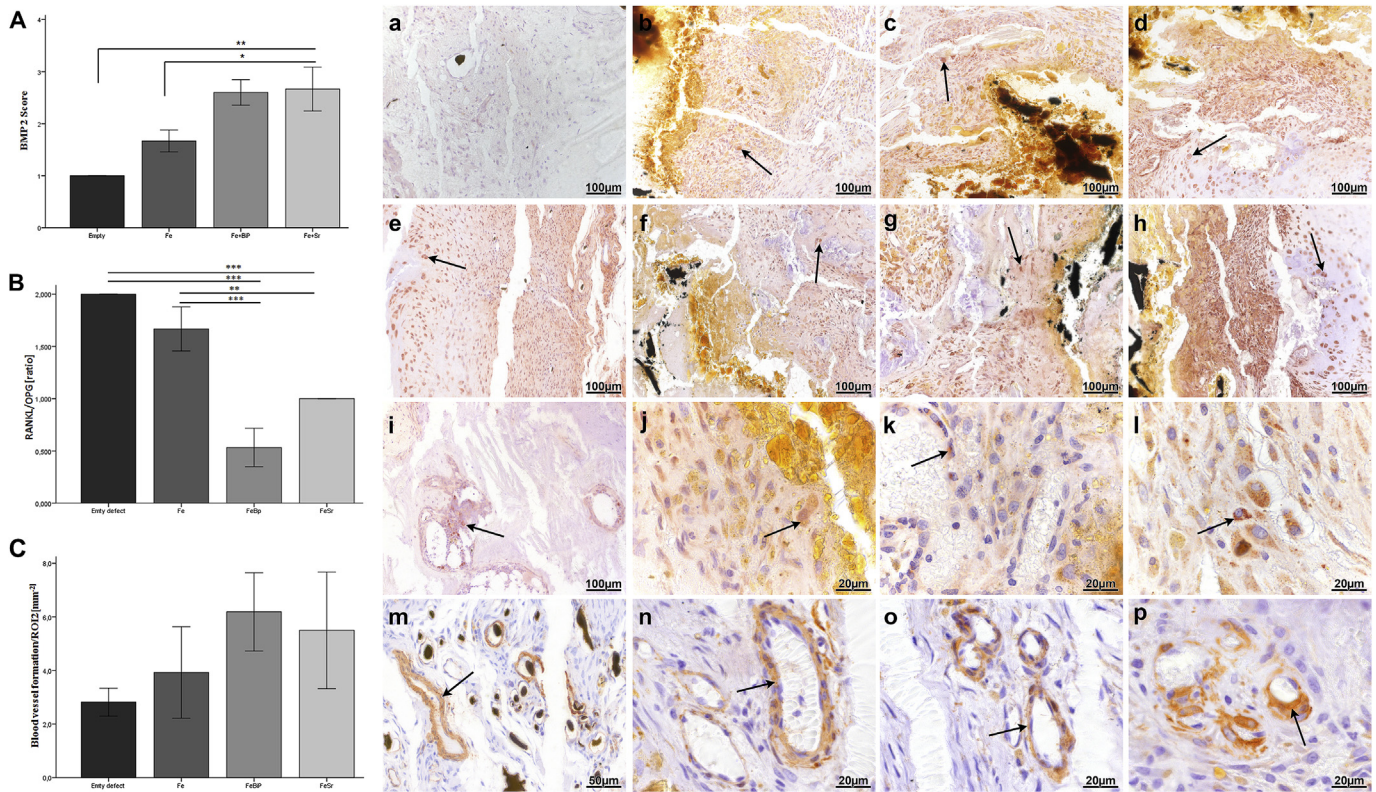
Fig. 5. Qualitative and quantitative analysis of immunohistochemical stain. Immunohistomorphometry of BMP2 (A; a-d), RANKL/OPG (B; e-l) and alpha smooth muscle actin (C; m-p) in empty defect, plain iron foam, FeBiP and FeSr respectively. Immunohistochemistry on undecalcified technovit sections showing an increased expression of potential biomarkers involved in bone formation in FeSr and FeBiP group. Increased expression of bone morphogenetic protein 2, BMP2; osteoprotegerin, OPG with simultaneous down-regulation of Receptor activator of nuclear factor kappa-B ligand, RANKL was seen at the tissue implant interface in the FeSr (c,g,k) and FeBiP group (d,h.l) in comparison to plain iron foam (b,f,j) and empty control group (a,e,i). No difference in blood vessel formation in between the empty, Fe, FeSr and FeBip (m,n,o,p). (n = 8 each, Man Whitney; (*) p < 0.05, (**) p < 0.01 and (***) p < 0.001 respectively).

In addition, RANKL/OPG ratio, an indicator for osteoclasto-genesis was significantly higher in the empty group when compared to FeBiP and FeSr respectively (p < 0.001). Also, a significantly higher RANKL/OPG ratio was seen in the plain iron foam when compared to FeBiP (p < 0.001) and FeSr (p = 0.018) respectively (Fig. 5B; e-l). Moreover, no differences in new blood vessel formation were seen when the empty defect was compared to Fe plain, FeSr, and FeBiP respectively. Interestingly there was a noticeable difference in the blood vessel size in between the groups (Fig. 5C; m-p). A significantly higher number of large-sized vessels were found in the Fe (p = 0.042) and FeSr (p = 0.030) group compared to FeBiP group (Supplementary Fig. S4). Middle-sized vessels were significantly higher in FeSr (p = 0.049) compared to FeBiP alone (Supplementary Fig. S4).

3.7. Gene expression analysis

The expressions of several genes (molecular markers of bone formation) were determined by qPCR. Results showed expression differences between the FeSr group and FeBiP group when compared to the empty defect group normalized to B2M gene expression. ALPL ($p = 0.005$), Runx2 ($p = 0.004$), Col1a1 ($p = 0.033$) and OCN ($p = 0.013$) were significantly down-regulated in iron foam with strontium (FeSr) in comparison to the empty defect group (C). Expression of Car2 was lower in the FeSr group ($p = 0.025$) and FeBiP ($p = 0.048$) when compared to the empty defect group (Fig. 6 D + F).

Additionally expression of ALPL ($p = 0.002$), Runx2 (p < 0.001), Col1a1 ($p = 0.035$) and OCN ($p = 0.022$), the potential molecular

markers for bone formation were lower in the FeBiP group when compared to the empty defect group (Fig. 6E). Gene expression analysis revealed no significant differences between the Fe plain group and the FeSr group, between the FeSr and the FeBiP group, between the Fe plain and the FeBiP group (Fig. 6G–L) and between the Fe plain and the empty defect group (Fig. 6A+B), respectively.

3.8. SEM/EDX

For a further elemental characterization of the bone sections with the implanted iron foams, we performed scanning electron microscopy along with EDX mappings. In Fig. 7 the SEM image of the section of foam coated with strontium carbonate phosphate is shown. As can be seen from the EDX mappings the iron foam still exists after 6 weeks and there is a remaining coating of strontium compound on the foam. In addition, also low amounts of calcium were found in the EDX mapping, which is an indicator that bio-mineralization started in the inner foam region. The maps also suggest for overlapping areas of Sr/Ca hydroxyapatite. From the Ca and P maps it can be concluded that in some areas already new bone has formed. Also, the Fe map shows that the iron has moved over a distance of more than 2 mm from the implant to the sur-rounding tissue.

3.9. Simulation of Sr^{2+} release from iron foam

Based on a model, which was introduced by Rohnke et al. for the release and transport of Sr^{2+} in bone from a strontium phosphate cement in vivo, we calculated the time-dependent Sr^{2+} release from
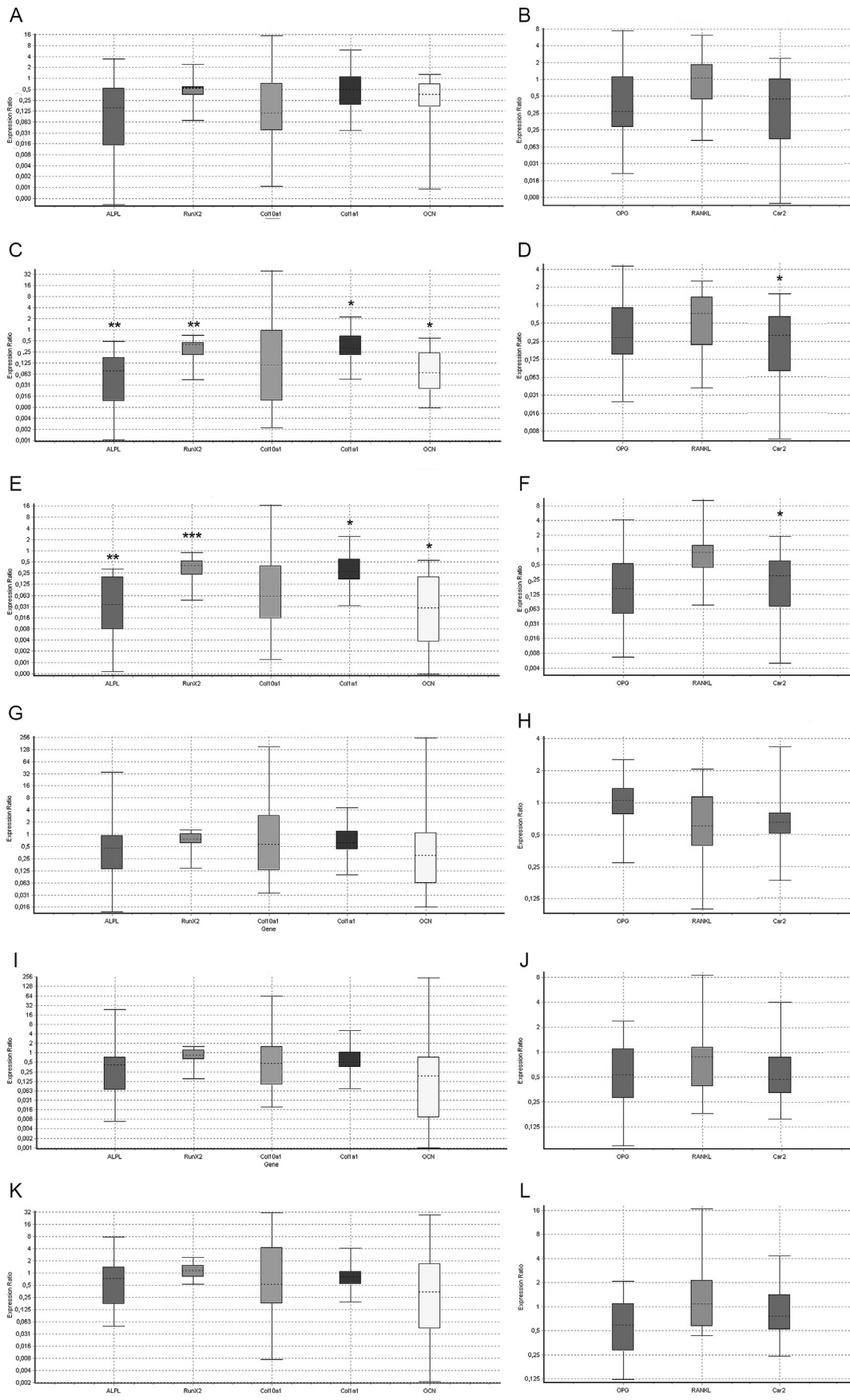
Fig. 6. Relative gene expression analysis. Between iron foam plain and empty defect as control group (A + B), iron foam with strontium (FeSr) and empty defect as control group (C + D), iron foam with bisphosphonate (FeBiP) and empty defect as control group (E + F), iron foam with strontium (FeSr) and iron foam plain (G + H) iron foam with bisphosphonate (FeBiP) and iron foam plain (I + J), iron foam with bisphosphonate (FeBiP) and iron foam with strontium (FeSr) (K + L). Alkaline phosphatase (ALP), Runt-related transcription factor 2 (Runx2), collagen type X alpha1 (Col10a1), osteocalcin (OCN) as bone formation markers (A, C, E, G, I, K). Receptor activator of nuclear factor kappa-B ligand (RANKL), osteoprotegerin (OPG) and carbonic anhydrase (Car2) as degradation markers (B, D, F, H, J, L). β2-microglobulin (B2M) was used as a reference gene. (n = 8 each, Student's t-test; (*) p < 0.05, (**) p < 0.01 and (***) p < 0.001 respectively).

the foam envelope [41]. For the release step a kinetics following $m(t) = 1.91*10^{-7}$ mol/cm^2*(t/h)$^{0.32}$ in combination with a pore diffusion coefficient of $D = 10^{-8}$ cm^2/s was applied, described earlier [41]. m(t) represents the released amount of Sr^{2+} per inner surface area of the foam. Fig. 7b shows the calculated overall Sr^{2+} release rate of the foam. After about 176 h the coating dissolved completely, which results in a kink in the release rate function. From this point, only pore diffusion is responsible for the further Sr^{2+} release rate from the foam envelope. In addition, the accumulated released Sr^{2+} mass is plotted. As can be seen, the release is still going on at t = 1.000 h (6 weeks), which is the duration of the *in vivo* experiment. In Fig. 7c the Sr^{2+} flux from the foam at t = 176.5 h is visualized in 3D. Fig. 7d represents one slice of the foam at t = 176.5 h. It can clearly be seen that there is a Sr^{2+} concentration gradient from the center to the envelope.

3.10. ToF-SIMS

ToF-SIMS analysis was done for all bone sections. No Fe and Sr signals were detected in the empty defect samples. Fig. 8 shows the mass images of bone sections with Fe foam with or without coatings of strontium and bisphosphonate. Within the RGB overlay Fe signal is given in blue, Ca in red and the distribution of the collagen fragment C$_4$H$_8$N$^+$ in green. Despite two exemptions, no calcium was found in the region of the foam. By comparing the mass image with the microscope image of the also given stained section it can be concluded that the Ag stained black area cannot be distinguished from the calcified area, which appears black, too. In contrast, the mass images of the sections with FeSr and FeBiP show more mineralized areas in the foam region. The group FeSr exhibits the highest degree of mineralization. In Fig. 8 exemplary line scans of the iron distribution within the sections are given. The x-axis is identical to the longitudinal axis of the femora. The data of the y-axis was summed up to improve statistics. It can be seen clearly that the degraded iron migrated through the complete bone in all three scaffold groups.

4. Discussion

Despite the known role of iron in human body metabolism,
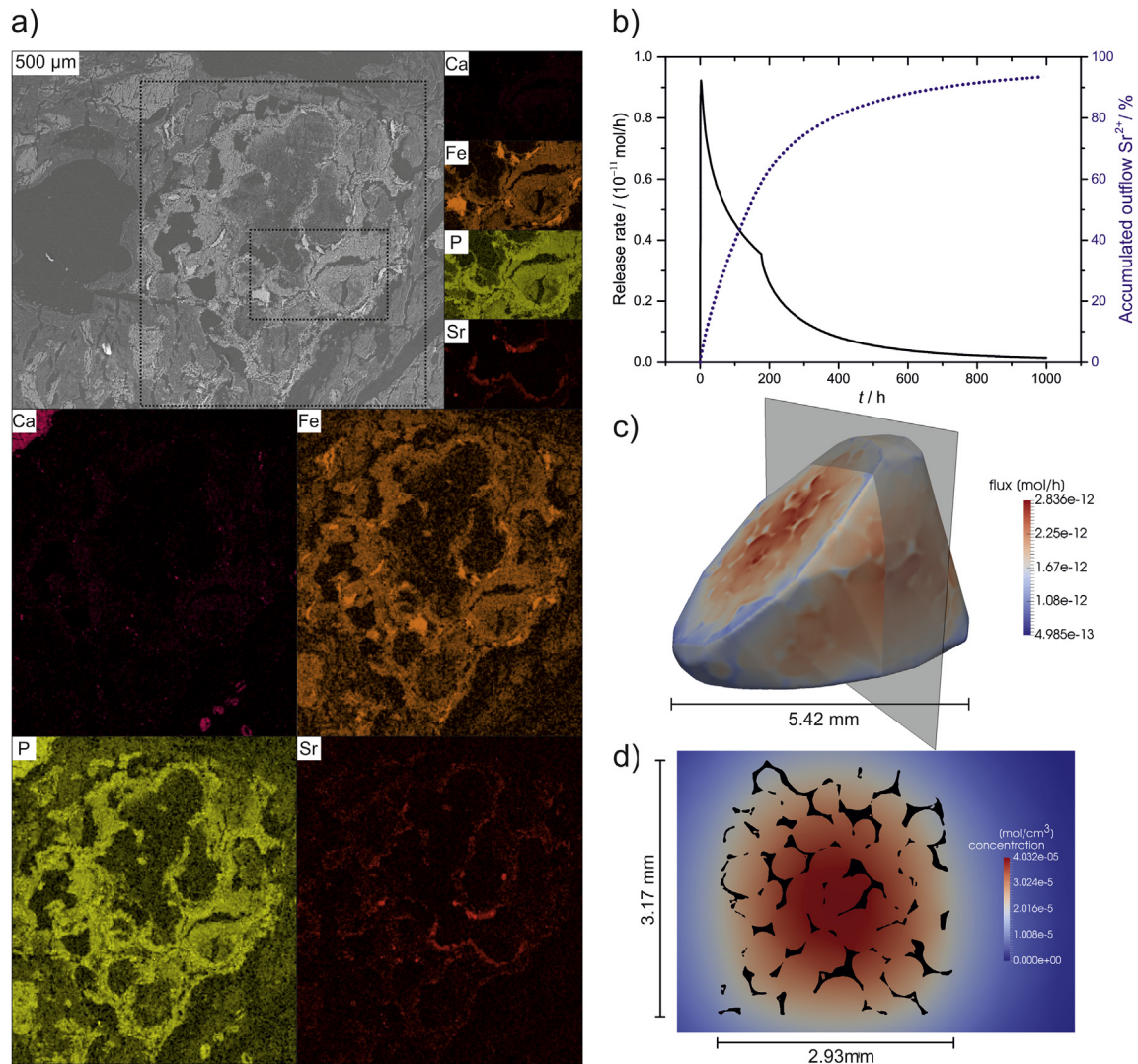
Fig. 7. SEM, EDX mappings and simulation of Sr^{2+} release a) SEM micrograph of Fe/Sr. Two areas are marked where EDX mappings were taken, a larger area and a smaller area within the larger. Resolution of the larger area is 284 × 340 data points with 180 frames, resolution of the smaller area is 256 × 192 data points with 150 frames. The intensities of the different elements are not normalized to each other; therefore, same intensities do not give same amounts. b) Calculated time dependent Sr^{2+} release rate (solid black line) and accumulated outflow of Sr^{2+} (blue doted line). c) 3D visualization of the Sr^{2+} flux from the foam at t = 176.5 h d) Slice through the foam at t = 176.5 h. (For interpretation of the references to color in this figure legend, the reader is referred to the Web version of this article.)
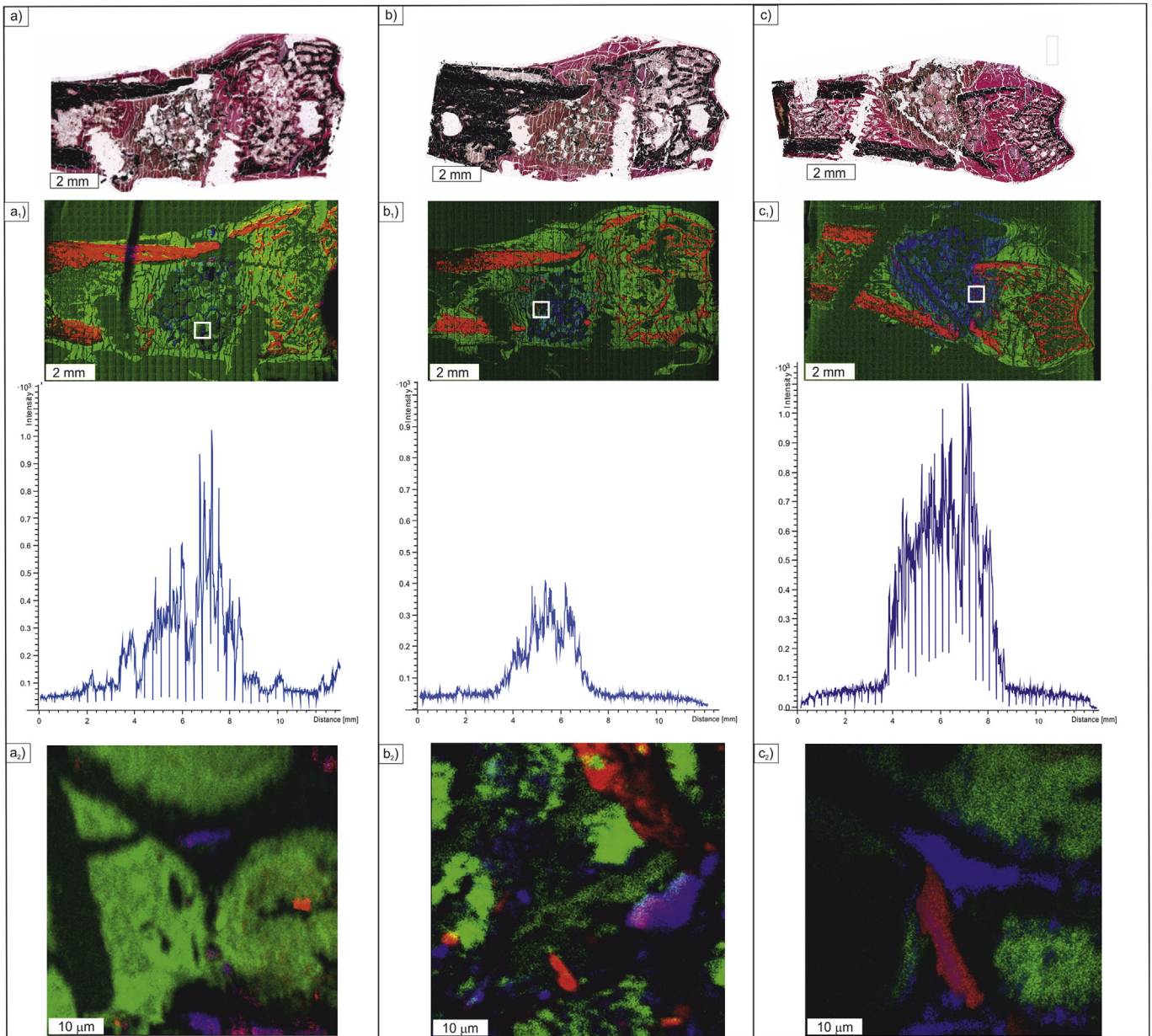
Fig. 8. Microscopic and ToF-SIMS images. Cross sections of rat femur after implantation of pure iron foam (a, a_1, a_2), iron foam with strontium (b, b_1, b_2) and iron foam with bisphosphonate (c, c_1, c_2). The microscopic images of the von Kossa and van Giessen stained samples (a, b, c) show the mineralized area in black, iron foam in brown and the soft tissue in purple. The ToF-SIMS images (a_1, b_1, c_1) are stage scans of the whole sections. Ca^+ is shown in red, Fe^+ in blue and the collagen fragment $C_4H_8N^+$ is given in green. The same color code accounts for the close up images of (a_2, b_2, c_2). Their origin is signed in the stage scans with white squares. The diagrams are line scans and show the distribution of the iron within the above given cross sections. Therefore, the iron signal intensity in y direction is summed up and plotted with the x-axis. (For interpretation of the references to color in this figure legend, the reader is referred to the Web version of this article.)

difficulties crop up when this material is employed as surgical implants due to the ferromagnetic behavior and the slow degradation rate associated with pure iron [45]. In addition, corrosion of implanted metallic biomedical devices may lead to the release of metal particles and ions which in turn may initiate adverse biological reactions and decrease biocompatibility and at times even lead to mechanical failure [46]. In lieu of this, the present work employed open cell iron foam structures coated with strontium and bisphosphonates to improve the environmental conditions in order to enhance bone formation and increase the biocompatibility. The coating further leads to enhanced bone formation markers at the protein level (IHC analyses) which in turn accentuate the bone healing process in the coated iron foams in comparison to the uncoated ones as well as the empty defect alone.

Anti-catabolic drugs such as strontium ranelate and bisphosphonates are the treatment alternatives for osteoporosis [47,48]. Strontium is known for its dual mode of action i. e enhance osteoblastogenesis and decrease osteoclastogenesis while bisphosphonates are known to inhibit osteoclast resorption thereby enhancing bone formation and thus improving the bone strength [49—51]. Despite the wide prescribed systemic administration of strontium ranelate for osteoporotic treatment, there are some concerns about its safety with potential vascular and neurological side-effects [52]. However, in the present study, a local targeted approach of Sr at a relatively low level (0.2mg/cm2) was applied by our biomaterial in contrast to the systemic

administration. Therefore, it can be assumed that the systemic concentration of Sr^{2+} is comparatively low, which avoids the mentioned side-effects. Thus strontium and bisphosphonates coated iron foams were substituted in a clinically relevant critical size metaphyseal fracture defect in an osteopenic bone and fracture healing was assessed. OVX-diet rat model used in this study is according to the FDA guidelines [53], well characterized and has been adopted previously to study material aided bone healing [31]. In addition, a 6-week time point post-implant substitution was chosen in accordance with the recommendation of Garcia et al. with reduced stress to animals [54].

Micro-Ct analysis in the present study reveals the substitution of Sr coating in Fe foam not only leads to a significant increase in bone formation at the interface region when compared to FeBiP and plain iron foam, but also an increase in bone formation was seen within the foams in FeSr group compared to plain Fe foam alone. This was further validated histomorphometrically showing increased bone formation at implant interface both in FeSr and FeBiP groups compared to plain Fe foam. Our group recently showed an enhanced bone volume over tissue volume in strontium substituted calcium phosphate (SrCPC) cements when compared to plain CPC and empty defect respectively [31]. These findings are also in line with the studies conducted by Baier et al. which showed strontium modified calcium phosphate cement enhances bone formation in critical size metaphyseal defect in OVX rats [55]. Yang et al. showed strontium containing alpha-calcium sulfate hemihydrate cement enhanced bone healing when substituted in a critical size calvarial defect in OVX rats [56]. Also, Amman et al. demonstrated the positive effects of strontium ranelate on bone architecture, the morphology of cortical and trabecular bone as well as the bone mass [57].

Strontium coating is also shown to improve implant osseointegration and in turn, enhances implant fixation in osteoporotic bone. Additionally, clinical studies have also shown alendronate to improve bone mineral density and reduce fracture risks [58]. Likewise, coatings of bisphosphonates have not only shown a positive effect on bone density but also reduce implant failure [59,60]. Local delivery of bisphosphonate using a polylactide glycolic acid copolymer also improved bone formation in vivo [61]. Researchers have also shown the local delivery of bisphosphonates from screw or titanium implants in vivo could improve bone density [62]. In the present study, the bisphosphonate coated iron foams showed a significantly higher bone volume over tissue volume in the entire defect region in comparison to the plain iron foam and empty defect group respectively. The increase in bone formation in case of FeSr and FeBiP could be correlated to the immunohistochemistry analysis which showed enhanced BMP2 and decreased RANKL/OPG levels.

The RANKL/OPG pathway is considered an important system of bone resorption [63]. The ratio is an important indicator whether bone resorption is enhanced or stunted. The immunohistochemical analysis of FeSr and FeBiP revealed an increased OPG expression with simultaneous down-regulation of RANKL levels when compared to plain iron foam and empty defect. No differences could, however, be seen in between strontium and bisphosphonates coated iron foams. Accordingly, the decreased RANKL/OPG ratio showed restricted osteoclastogenesis thereby reducing bone resorption. Studies show the osteoanabolic effect of strontium leads to enhanced OPG, which in turn blocks the RANK/RANKL pathway thereby inhibiting osteoclastogenesis. In an in vitro study Greiner et al. also showed bisphosphonates decreases the RANKL/OPG ratio [64]. The relative expression data, however, did not reveal any significant difference between the groups.

This result was expected as the time point for evaluation i.e. 6 weeks represents the early healing stage and the material

substitution in osteoporotic fractured bones could not lead it to a remodeling stage. Interestingly, Car2 was significantly downregulated in FeSr and FeBiP group compared to the empty defect group. Carbonic anhydrase (Car2) is considered to play a major role in bone resorption and its decreased expression in the strontium and bisphosphonates substituted groups confers the decrease in osteoclast activity in comparison to the empty defect. Intriguingly, gene expression analysis revealed a significant downregulation of the molecular markers of bone formation in the FeSr and FeBiP group when compared to the empty defect. This restricted viability of the osteoblast activity could be attributed to the released metal ions as shown by Hallab et al. [65]. However, the enzyme histochemistry revealed a significant increase in the osteoblast surface both in the FeSr and FeBiP group with a simultaneous downregulation of osteoclast activity.

The influence of material environment on cells and vice versa is of great importance. Our approach of TOF-SIMS together with the visualization of the osteoblast, osteoclast, and osteocytes reveal a correlation between mineralized bone tissue and the cell behavior. Chondrocytes, osteoblast, and osteocytes play a crucial role in bone healing and formation. The proliferation and regulation of these cells are however determined by the differentiation ability of mesenchymal stem cells. Despite the osteoporotic bone status which affects vital pathways of cell survival and differentiation such as ERK and Wnt pathways, the treatment has shown enhanced proliferation of mesenchymal origin cells. Osteoblasts which help in the bone matrix formation were found to be highest in FeSr and FeBiP which showed areas of high mineralization with a simultaneous increase in ALP expression levels as revealed by the IHC analysis. This was further confirmed by the SEM EDX analysis which showed overlapping areas of Ca, P and Sr. Also the osteocyte network architecture has been shown to be correlated with bone material quality by directly controlling bone mineral in their vicinity [66]. The well-organized osteocytic lacuna canaliculi system (OLCS) may also provide access to the mineralized bone matrix thereby leading to higher bone material quality around the implants.

Drug release from the foam should be divided into two mechanistic steps. First, the release step from the coating layer followed by pore diffusion. For a realistic release experiment, it would be necessary to fill the foam pore structure with body fluid or bone marrow, respectively to obtain the right pore diffusion coefficient. The latter is technically challenging and was never described in the literature. Due to the fact, that in vitro life like release experiments of Sr^{2+} or zoledronate from the iron foam cannot be performed, we decided to carry out a 3D simulation for the Sr^{2+} release. Although we used a simple model for the overall release kinetics, it fits quite well with the in vivo observations. In most pores, the coating is dissolved. However, some areas with strontium minerals were also found. This might be due to an inhomogeneous coating thickness or ongoing biomineralization in the foam. In addition, a release of strontium could still be seen at 6 weeks (1000 h) which matches ours in vivo experiment. However, a distinct statement is not possible with the existing experimental results. It might be also assumed that the time-dependent bisphosphonate release is similar but again we have no distinct evidence.

Vascularization is also one of the key factors for the success of a bone graft material. Metal foams meet these criteria due to their open structure porosity which allows bony in growth. Although there was no significant difference in the number of blood vessels between the groups, vessels with smaller diameter were found in the FeBiP group. The observed difference is in accordance with studies that show strontium stimulates angiogenesis by increasing the expression of growth factors such as VEGF [67,68]. In contrast, bisphosphonates have an anti-angiogenic effect. In vitro and in vivo

studies show mature vascular and endothelial progenitor cells are very sensitive to nitrogen-containing bisphosphonates. Hasmim et al. also showed zoledronate inhibits adhesion, spread and survival of endothelial cells [69].

Finally, the progressive osseointegration on one hand and material degradation on the other, guarantee an optimal adaptation to the corresponding strength state at any time [70]. The porous iron foam enabled blood vessel formation along with osseointegration in all the groups. However, the highest amount of osseous tissue was seen in the FeSr pores. The presence of strontium thus ameliorated osseous-integration of iron foam and therefore fracture healing [71]. Also for the iron-based implant, a temporary bioactive coating reduces the early potential cytotoxic effects of corrosion products detriment for bony integration of an implant material [72]. Thus the osteoconductivity of strontium and bisphosphonate coatings not only provided the scope for bony ingrowth but seems to have also protected from preliminary detrimental effects of corrosion products of iron if any. Moreover, experimental data from Glorius et al. showed the iron component only start to corrode after the mineral matrix gets removed. Biocorrosion analysis showed a significant increased biocorrosion/implant retention in FeSr and FeBiP compared to plain Fe also opens up the scope to combine an osteoconductive cement matrix with a bio-corrodable reinforcement. Nevertheless, in the present work, no significant changes of the degradation were observed. However, further increasing the corrosion rate of FeSr and FeBiP group could answer the limitation of slow *in vivo* degradation.

Plate failure as seen in this study can be considered as a drawback. However, this also reflects the clinical challenge of osteoporotic patients with non-healing fractures. Nevertheless, a trend with almost no or less plate failure was seen in case of FeSr and FeBiP group which demonstrate better bone healing parameters when compared to plain iron and empty defect groups. This could be further substantiated by the increased BV/TV as seen in case of both the groups compared to plain Fe and empty defect. The major limitation of this *in vivo* study was the choice of only one-time point of 6 weeks' and that no significant differences in degradation rates could be assessed. Since it is generally accepted that 6 weeks' time point represents an early stage of bone healing and none of the coatings could have enhanced the osteoporotic bone healing to a completely remodeled state, longer time point must be assessed. Although the study results indicate integration at bone/material interface, a clear functional benefit and detailed understanding to molecular regulation during the healing is absent. However, the goal of the study was to describe healing at the critical reparative phase of 6 weeks. The use of further animals to study the molecular regulation and consolidation at earlier and later time points is the focus of future studies. Nonetheless, further in detail analysis of functional benefit using collagen fiber structure analysis in TEM images that correlates to bone quality will also benefit development of tissue-engineered constructs. Also, since a balance between biomaterial degradation and cell functions is essential for targeted tissue formation [73], future research needs to focus to strike a balance between the two.

5. Conclusion

The application of iron as a scaffold material for tissue engineering is limited. The present study shows that open cell iron foams coated with strontium and bisphosphonates enhance bone formation as compared to plain foams or empty defect. The coatings thus enhanced the bioactivity by increasing prominent bone formation markers. With the known mechanical properties of iron to that of bone, iron-based materials are a promising approach for the design of new load-bearing synthetic bone graft substitutes.

Nevertheless, further research has to be done on increasing the biocorrosion. Further understanding of the influence of porous structure on tissue and cell regeneration, mechanical and degradation properties, as well as product transport and vascularization could lead to the development of novel osteoconductive bone graft substitutes.

Appendix A. Supplementary data

Supplementary data related to this article can be found at https://doi.org/10.1016/j.biomaterials.2017.11.049.

References

[1] Y. Liu, G. Wu, K. de Groot, Biomimetic coatings for bone tissue engineering of critical-sized defects, J. R. Soc. Interface 7 (2010) S631–S647.

[2] A.R. Amini, C.T. Laurencin, S.P. Nukavarapu, Bone tissue engineering: recent advances and challenges, Crit. Rev. Biomed. Eng. 40 (2012) 363–408.

[3] S.R. Caliari, M.A. Ramirez, B.A.C. Harley, The development of collagen-GAG scaffold-membrane composites for tendon tissue engineering, Biomaterials 32 (2011) 8990–8998.

[4] F.J. O'Brien, Biomaterials & scaffolds for tissue engineering, Mater. Today 14 (2011) 88–95.

[5] A.H. Yusop, A.A. Bakir, N.A. Shaharom, M.R. Abdul Kadir, H. Hermawan, Porous biodegradable metals for hard tissue scaffolds: a review, Int. J. Biomaterials 2012 (2012) 641430.

[6] G.M. Cunniffe, F.J. O'Brien, Collagen scaffolds for orthopedic regenerative medicine, JOM 63 (2011) 66.

[7] F.G. Lyons, A.A. Al-Munajjed, S.M. Kieran, M.E. Toner, C.M. Murphy, G.P. Duffy, et al., The healing of bony defects by cell-free collagen-based scaffolds compared to stem cell-seeded tissue engineered constructs, Biomaterials 31 (2010) 9232–9243.

[8] M.N. Rahaman, D.E. Day, B.S. Bal, Q. Fu, S.B. Jung, L.F. Bonewald, et al., Bioactive glass in tissue engineering, Acta Biomater. 7 (2011) 2355–2373.

[9] P.V. Giannoudis, T.A. Einhorn, D. Marsh, Fracture healing: the diamond concept, Injury 38 (2007) S3–S6.

[10] G. Papavasiliou, M.-H. Cheng, E.M. Brey, Strategies for vascularization of polymer scaffolds. Journal of investigative medicine, Offic. Publ. Am. Fed. Clin. Res. 58 (2010) 838–844.

[11] H. Li, Y. Zheng, L. Qin, Progress of biodegradable metals, Prog. Nat. Sci. Mater. Int. 24 (2014) 414–422.

[12] H. Hermawan, D. Dube, D. Mantovani, Degradable metallic biomaterials: design and development of Fe-Mn alloys for stents, J. Biomed. Mater Res. A 93 (2010) 1–11.

[13] H. Hermawan, D. Dube, D. Mantovani, Developments in metallic biodegradable stents, Acta Biomater. 6 (2010) 1693–1697.

[14] H. Hermawan, A. Purnama, D. Dube, J. Couet, D. Mantovani, Fe–Mn alloys for metallic biodegradable stents: degradation and cell viability studies, Acta Biomater. 6 (2010) 1852–1860.

[15] D. Vojtěch, J. Kubásek, J. Šerák, P. Novák, Mechanical and corrosion properties of newly developed biodegradable Zn-based alloys for bone fixation, Acta Biomater. 7 (2011) 3515–3522.

[16] H. Kitabata, R. Waksman, B. Warnack, Bioresorbable metal scaffold for cardiovascular application: current knowledge and future perspectives, Cardiovasc. Revascularization Med. 15 (2014) 109–116.

[17] F. Witte, F. Feyerabend, P. Maier, J. Fischer, M. Störmer, C. Blawert, et al., Biodegradable magnesium–hydroxyapatite metal matrix composites, Biomaterials 28 (2007) 2163–2174.

[18] S.Y. Cho, S.W. Chae, K.W. Choi, H.K. Seok, Y.C. Kim, J.Y. Jung, et al., Biocompatibility and strength retention of biodegradable Mg-Ca-Zn alloy bone implants, J. Biomed. Mater Res. B Appl. Biomater. 101 (2013) 201–212.

[19] Y.B. Wang, X.H. Xie, H.F. Li, X.L. Wang, M.Z. Zhao, E.W. Zhang, et al., Biodegradable CaMgZn bulk metallic glass for potential skeletal application, Acta Biomater. 7 (2011) 3196–3208.

[20] Z. Li, X. Gu, S. Lou, Y. Zheng, The development of binary Mg-Ca alloys for use as

biodegradable materials within bone, Biomaterials 29 (2008) 1329—1344.

[21] M.S. Uddin, H. Colin, M. Peter, Surface treatments for controlling corrosion rate of biodegradable Mg and Mg-based alloy implants, Sci. Technol. Adv. Mater. 16 (2015), 053501.

[22] U. Thormann, V. Alt, L. Heimann, C. Gasquere, C. Heiss, G. Szalay, et al., The biocompatibility of degradable magnesium interference screws: an experimental study with sheep, BioMed Res. Int. 2015 (2015) 943603.

[23] B.S. Moonga, D.W. Dempster, Zinc is a potent inhibitor of osteoclastic bone resorption in vitro, J. Bone Min. Res. 10 (1995) 453—457.

[24] M. Moravej, D. Mantovani, Biodegradable metals for cardiovascular stent application: interests and new opportunities, Int. J. Mol. Sci. 12 (2011) 4250—4270.

[25] M. Peuster, C. Hesse, T. Schloo, C. Fink, P. Beerbaum, C. von Schnakenburg, Long-term biocompatibility of a corrodible peripheral iron stent in the porcine descending aorta, Biomaterials 27 (2006) 4955—4962.

[26] B. Liu, Y.F. Zheng, Effects of alloying elements (Mn, Co, Al, W, Sn, B, C and S) on biodegradability and in vitro biocompatibility of pure iron, Acta Biomater. 7 (2011) 1407—1420.

[27] G.J. Thompson, D.A. Puleo, Effects of sublethal metal ion concentrations on osteogenic cells derived from bone marrow stromal cells, J. Appl. Biomater. 6 (1995) 249—258.

[28] F.L. Nie, Y.F. Zheng, S.C. Wei, C. Hu, G. Yang, In vitro corrosion, cytotoxicity and hemocompatibility of bulk nanocrystalline pure iron, Biomed. Mater. 5 (2010) 1748—6041.

[29] F. Matassi, A. Botti, L. Sirleo, C. Carulli, M. Innocenti, Porous metal for orthopedics implants, Clin. Cases Mineral Bone Metabolism 10 (2013) 111—115.

[30] G.M. Kuang, W.P. Yau, J. Wu, K.W. Yeung, H. Pan, W.M. Lam, et al., Strontium exerts dual effects on calcium phosphate cement: accelerating the degradation and enhancing the osteoconductivity both in vitro and in vivo, J. Biomed. Mater. Res. Part A 103 (2015) 1613—1621.

[31] U. Thormann, S. Ray, U. Sommer, T. Elkhassawna, T. Rehling, M. Hundgeburth, et al., Bone formation induced by strontium modified calcium phosphate cement in critical-size metaphyseal fracture defects in ovariectomized rats, Biomaterials 34 (2013) 8589—8598.

[32] M.T. Drake, B.L. Clarke, S. Khosla, Bisphosphonates: mechanism of action and role in clinical practice, Mayo Clin. Proc. Mayo Clin. 83 (2008) 1032—1045.

[33] G. Manivasagam, D. Durgalakshmi, Rajamanickam Asokamani, Biomedical implants: corrosion and its prevention - a review, Recent Pat. Corros. Sci. (January 2010) 40—54.

[34] T. El Khassawna, W. Böcker, P. Govindarajan, N. Schliefke, B. Hürter, M. Kampschulte, et al., Effects of multi-deficiencies-diet on bone parameters of peripheral bone in ovariectomized mature rat, PLoS ONE 8 (2013), e71665.

[35] V. Alt, U. Thormann, S. Ray, D. Zahner, L. Durselen, K. Lips, et al., A new metaphyseal bone defect model in osteoporotic rats to study biomaterials for the enhancement of bone healing in osteoporotic fractures, Acta Biomater. 9 (2013) 7035—7042.

[36] M.L. Bouxsein, S.K. Boyd, B.A. Christiansen, R.E. Guldberg, K.J. Jepsen, R. Muller, Guidelines for assessment of bone microstructure in rodents using micro-computed tomography, J. Bone Min. Res. 25 (2010) 1468—1486.

[37] J. Albers, J. Schulze, F.T. Beil, M. Gebauer, A. Baranowsky, J. Keller, et al., Control of bone formation by the serpentine receptor Frizzled-9, J. Cell Biol. 192 (2011) 1057—1072.

[38] A. Peters, D. Toben, J. Lienau, H. Schell, H.J. Bail, G. Matziolis, et al., Locally applied osteogenic predifferentiated progenitor cells are more effective than undifferentiated mesenchymal stem cells in the treatment of delayed bone healing, Tissue Eng. Part A 15 (2009) 2947—2954.

[39] T. El Khassawna, D.E.S. Daghma, S. Stoetzel, S. Ray, S. Kern, D. Malhan, et al., Postembedding decalcification of mineralized tissue sections preserves the integrity of implanted biomaterials and minimizes number of experimental animals, BioMed Res. Int. 2017 (2017) 10.

[40] H. Hermawan, D. Dubé, D. Mantovani, Degradable metallic biomaterials: design and development of Fe—Mn alloys for stents, J. Biomed. Mater. Res. Part A 93A (2010) 1—11.

[41] M. Rohnke, S. Pfitzenreuter, B. Mogwitz, A. Henß, J. Thomas, D. Bieberstein, et al., Strontium release from Sr2+-loaded bone cements and dispersion in healthy and osteoporotic rat bone, J. Control. Release 262 (2017) 159—169.

[42] X. Li, J. Lowengrub, A. Rätz, A. Voigt, Solving pdes in complex geometries, Commun. Math. Sci. 7 (2009) 81—107.

[43] S. Vey, A. Voigt, AMDiS: adaptive multidimensional simulations, Comput. Vis. Sci. 10 (2007) 57—67.

[44] T. Witkowski, S. Ling, S. Praetorius, A. Voigt, Software concepts and numerical algorithms for a scalable adaptive parallel finite element method, Adv. Comput. Math. 41 (2015) 1145—1177.

[45] A.H. Yusop, A.A. Bakir, N.A. Shaharom, M.R. Abdul Kadir, H. Hermawan, Porous biodegradable metals for hard tissue scaffolds: a review, Int. J. Biomaterials 2012 (2012) 10.

[46] J.J. Jacobs, J.L. Gilbert, R.M. Urban, Corrosion of metal orthopaedic implants, J. Bone Jt. Surg. Am. 80 (1998) 268—282.

[47] G.P. Lyritis, T. Georgoulas, C.P. Zafeiris, Bone anabolic versus bone anti-catabolic treatment of postmenopausal osteoporosis, Ann. N. Y. Acad. Sci. 1205 (2010) 277—283.

[48] J.M.R. Mathoo, L. Becker, D. Kumbhare, J.D. Adachi, Therapeutic advances in the treatment of osteoporosis, Expert Opin. Ther. Pat. 17 (2007) 277—285.

[49] P.J. Marie, D. Felsenberg, M.L. Brandi, How strontium ranelate, via opposite effects on bone resorption and formation, prevents osteoporosis, Osteoporos. Int. 22 (2011) 1659—1667.

[50] E. van der Poest Clement, P. Patka, K. Vandormael, H. Haarman, P. Lips, The effect of alendronate on bone mass after distal forearm fracture, J. Bone Min. Res. 15 (2000) 586—593.

[51] M.P. Watkins, J.Y. Norris, S.K. Grimston, X. Zhang, R.J. Phipps, F.H. Ebetino, et al., Bisphosphonates improve trabecular bone mass and normalize cortical thickness in ovariectomized, osteoblast connexin43 deficient mice, Bone 51 (2012) 787—794.

[52] S. O'Donnell, A. Cranney, G.A. Wells, J. Adachi, J.-Y. Reginster, Strontium ranelate for preventing and treating postmenopausal osteoporosis, Cochrane Database Syst. Rev. (3) (2006), CD005326, https://doi.org/10.1002/14651858.CD005326.pub2.

[53] D.D. Thompson, H.A. Simmons, C.M. Pirie, H.Z.F.D.A. Ke, Guidelines and animal models for osteoporosis, Bone 17 (1995) 125s—133s.

[54] P. Garcia, T. Histing, J.H. Holstein, M. Klein, M.W. Laschke, R. Matthys, et al., Rodent animal models of delayed bone healing and non-union formation: a comprehensive review, Eur. Cell Mater. 26 (2013) 1—12 discussion -4.

[55] M. Baier, P. Staudt, R. Klein, U. Sommer, R. Wenz, I. Grafe, et al., Strontium enhances osseointegration of calcium phosphate cement: a histomorphometric pilot study in ovariectomized rats, J. Orthop. Surg. Res. 8 (2013) 16.

[56] S. Yang, L. Wang, S. Feng, Q. Yang, B. Yu, M. Tu, Enhanced bone formation by strontium modified calcium sulfate hemihydrate in ovariectomized rat critical-size calvarial defects, Biomed. Mater. (2017) 12.

[57] P. Ammann, V. Shen, B. Robin, Y. Mauras, J.P. Bonjour, R. Rizzoli, Strontium ranelate improves bone resistance by increasing bone mass and improving architecture in intact female rats, J. Bone Min. Res. 19 (2004) 2012—2020.

[58] J.E. Brouwers, F.M. Lambers, J.A. Gasser, B. van Rietbergen, R. Huiskes, Bone degeneration and recovery after early and late bisphosphonate treatment of ovariectomized wistar rats assessed by in vivo micro-computed tomography, Calcif. Tissue Int. 82 (2008) 202—211.

[59] P. Tengvall, B. Skoglund, A. Askendal, P. Aspenberg, Surface immobilized bisphosphonate improves stainless-steel screw fixation in rats, Biomaterials 25 (2004) 2133—2138.

[60] Y. Gao, S. Zou, X. Liu, C. Bao, J. Hu, The effect of surface immobilized bisphosphonates on the fixation of hydroxyapatite-coated titanium implants in ovariectomized rats, Biomaterials 30 (2009) 1790—1796.

[61] B. Peter, D.P. Pioletti, S. Laib, B. Bujoli, P. Pilet, P. Janvier, et al., Calcium phosphate drug delivery system: influence of local zoledronate release on bone implant osteointegration, Bone 36 (2005) 52—60.

[62] A. Roshan-Ghias, J. Arnoldi, P. Procter, D.P. Pioletti, In vivo assessment of local effects after application of bone screws delivering bisphosphonates into a compromised cancellous bone site, Clin. Biomech. 26 (2011) 1039—1043.

[63] B.F. Boyce, L. Xing, Biology of RANK, RANKL, and osteoprotegerin, Arthritis Res. Ther. 9 (Suppl 1) (2007) S1.

[64] S. Greiner, A. Kadow-Romacker, M. Lubberstedt, G. Schmidmaier, B. Wildemann, The effect of zoledronic acid incorporated in a poly(D,L-lactide) implant coating on osteoblasts in vitro, J. Biomed. Mater Res. A 80 (2007) 769—775.

[65] N.J. Hallab, C. Vermes, C. Messina, K.A. Roebuck, T.T. Glant, J.J. Jacobs, Concentration- and composition-dependent effects of metal ions on human MG-63 osteoblasts, J. Biomed. Mater Res. 60 (2002) 420—433.

[66] M. Kerschnitzki, P. Kollmannsberger, M. Burghammer, G.N. Duda, R. Weinkamer, W. Wagermaier, et al., Architecture of the osteocyte network correlates with bone material quality, J. bone mineral Res. Offic J. Am. Soc. Bone Mineral Res. 28 (2013) 1837—1845.

[67] F. Liu, X. Zhang, X. Yu, Y. Xu, T. Feng, D. Ren, In vitro study in stimulating the secretion of angiogenic growth factors of strontium-doped calcium polyphosphate for bone tissue engineering, J. Mater Sci. Mater Med. 22 (2011) 683—692.

[68] P. Kang, X. Xie, Z. Tan, J. Yang, B. Shen, Z. Zhou, et al., Repairing defect and preventing collapse of femoral head in a steroid-induced osteonecrotic of femoral head animal model using strontium-doped calcium polyphosphate combined BM-MNCs, J. Mater Sci. Mater Med. 26 (2015) 80.

[69] M. Hasmim, G. Bieler, C. Ruegg, Zoledronate inhibits endothelial cell adhesion, migration and survival through the suppression of multiple, prenylation-dependent signaling pathways, J. Thromb. Haemost. 5 (2007) 166—173.

[70] B. Wegener, B. Sievers, S. Utzschneider, P. Müller, V. Jansson, S. Rößler, et al., Microstructure, cytotoxicity and corrosion of powder-metallurgical iron alloys for biodegradable bone replacement materials, Mater. Sci. Eng. B 176 (2011) 1789—1796.

[71] K.S. Lips, V. Kauschke, S. Hartmann, U. Thormann, S. Ray, M. Kampschulte, et al., Podoplanin immunopositive lymphatic vessels at the implant interface in a rat model of osteoporotic fractures, PLoS One 8 (2013), e77259.

[72] S. Glorius, B. Nies, J. Farack, P. Quadbeck, R. Hauser, G. Standke, et al., Metal foam — bone cement composites: mechanical and biological properties and perspectives for bone implant design, Adv. Eng. Mater. 13 (2011) 1019—1023.

[73] L.C. Abraham, J.F. Dice, P.F. Finn, N.T. Mesires, K. Lee, D.L. Kaplan, Extracellular matrix remodeling—methods to quantify cell-matrix interactions, Biomaterials 28 (2007) 151—161.